

Inert sextuplet scalar dark matter at the LHC and future colliders

Dan-Yang Liu, Chengfeng Cai, Zhao-Huan Yu,^{*} Yu-Pan Zeng, and Hong-Hao Zhang[†]

School of Physics, Sun Yat-Sen University, Guangzhou 510275, China

We study a dark matter model constructed by extending the standard model with an inert $SU(2)_L$ sextuplet scalar of hypercharge $1/2$. The sextuplet components are split by the quartic couplings between the sextuplet and the Higgs doublet after electroweak symmetry breaking, resulting in a dark sector with one triply charged, two doubly charged, two singly charged, and two neutral scalars. The lighter neutral scalar boson acts as a dark matter particle. We investigate the constraints on this model from the monojet + \cancel{E}_T and soft-dilepton + jets + \cancel{E}_T searches at the 13 TeV Large Hadron Collider, as well as from the current electroweak precision test. Furthermore, we estimate the projected sensitivities of a 100 TeV pp collider and of a future e^+e^- collider, and find that such future projects could probe TeV mass scales.

arXiv:2008.06821v1 [hep-ph] 16 Aug 2020

^{*} yuzhaoh5@mail.sysu.edu.cn

[†] zh98@mail.sysu.edu.cn

CONTENTS

I. Introduction	3
II. Inert sextuplet scalar model	4
III. Mass splittings and scalar decays	7
IV. Searches at pp colliders	11
A. Monojet + \cancel{E}_T channel	13
1. LHC constraint	14
2. 100 TeV pp collider sensitivity	15
B. Soft-dilepton + jets + \cancel{E}_T channel	17
1. LHC constraint	18
2. 100 TeV pp collider sensitivity	19
V. Indirect probe with electroweak oblique parameters	22
VI. Conclusions	26
Acknowledgments	27
A. Electroweak gauge couplings of the sextuplet scalar	27
B. Vacuum polarizations of electroweak gauge bosons	28
References	29

I. INTRODUCTION

The standard model (SM) of particle physics is a self-consistent $SU(3)_C \times SU(2)_L \times U(1)_Y$ gauge theory describing the properties and interactions of three generations of fundamental fermions [1–3]. It has been well tested by a variety of experiments, and all the fundamental particles it predicts have been found. However, the SM cannot explain the existence of cold dark matter (DM) in the Universe, which is strongly suggested by astrophysical and cosmological experiments [4–6]. In order to account for particle dark matter, the SM must be extended.

Many popular extensions involve weakly interacting massive particles (WIMPs) as DM candidates, since thermal production of WIMPs in the early Universe is typically consistent with the observation of DM relic abundance. From the viewpoint of model building, WIMP models can be directly established by introducing extra colorless $SU(2)_L$ multiplets as the dark sector [7–59]. The lightest mass eigenstate from the electrically neutral components of the multiplets could be a viable DM candidate, which can be either a fermion or scalar boson. In order to ensure the stability of the DM candidate, a Z_2 symmetry is commonly required.

In this way, scalar DM models can be constructed by extending the scalar sector with an inert scalar multiplet that does not develop a vacuum expectation value (VEV) because of an unbroken Z_2 symmetry. Such extensions with doublet [9, 10, 12, 60], triplet [11, 13, 15, 16, 19, 21, 25, 33, 56–58], quadruplet [21, 37, 38, 55], quintuplet [11, 15, 20, 42, 51], sextuplet [20, 23, 34], septuplet [11, 15, 18, 20, 29, 30, 51], and octuplet [20, 23, 34] scalars have been discussed in the literature.

In this work, we focus on the case of an inert sextuplet scalar with hypercharge $Y = 1/2$. A previous study [23] on this case investigated the phenomenological constraints from unitarity, electroweak oblique parameters, loop-induced Higgs decays into $\gamma\gamma$ and $Z\gamma$, DM relic abundance, and DM direct detection. A follow-up work [34] analyzed the impact of coannihilation and Sommerfeld enhancement effects on the relic abundance calculation, as well as the scale where a Landau pole appears. Here we extend these studies to the searches for the sextuplet scalar at the Large Hadron Collider (LHC) and future colliders.

After electroweak symmetry breaking, the mass eigenstates from the sextuplet scalar involve one triply charged scalar, two doubly charged scalars, two singly charged scalars, and two neutral scalars. The lighter neutral scalar boson acts as a DM candidate. At a high energy pp collider, the scalar bosons could be directly produced in pairs via electroweak interactions. Their decay chains would end at the DM candidate, which escapes detection and typically leaves a large missing transverse energy (\cancel{E}_T). Potential searching channels in pp collisions include the monojet + \cancel{E}_T and soft-dilepton + jets + \cancel{E}_T final states.

We will investigate the constraints from current LHC searches. Moreover, the international high energy physics community is proposing future pp collider projects, such as the Super Proton-Proton Collider (SPPC) at $\sqrt{s} \sim 70$ –100 TeV [61] and the pp Future Cir-

cular Collider at $\sqrt{s} \sim 100$ TeV [62]. We will explore the prospect at a future 100 TeV pp collider based on simulation. Furthermore, electroweak interactions of the dark sector scalars also affect the electroweak oblique parameters at loop level, which can be examined in the electroweak precision test (EWPT). Future e^+e^- collider projects, such as the Circular Electron-Positron Collider (CEPC) [63], the e^+e^- Future Circular Collider [64], and the International Linear Collider [65], have plans to precisely measure the properties of the Z , W , and Higgs bosons and the top quark. These measurements would greatly improve the determination of the electroweak oblique parameters [66]. We will estimate the corresponding sensitivity.

The paper is organized as follows. In Sec. II, we introduce the inert sextuplet scalar model. In Sec. III, we discuss the mass spectrum and decay processes. In Sec. IV, we investigate the current constraints from the monojet + \cancel{E}_T and soft-dilepton + jets + \cancel{E}_T searches at the LHC and the sensitivity at a 100 TeV pp collider. In Sec. V, we explore the current EWPT constraint and the future CEPC sensitivity. In Sec. VI, we give the conclusions.

II. INERT SEXTUPLET SCALAR MODEL

In the inert sextuplet scalar model, the SM is extended with a $SU(2)_L$ sextuplet scalar field S of hypercharge $Y = 1/2$ [23, 34], which can be expressed as

$$\begin{aligned} S &= (S^{3+}, S^{2+}, S^+, S^0, S^-, S^{2-})^T \\ &= \left(S^{11111}, \sqrt{5}S^{11112}, \sqrt{10}S^{11122}, \sqrt{10}S^{11222}, \sqrt{5}S^{12222}, S^{22222} \right)^T. \end{aligned} \quad (1)$$

In the first line, the S components are labeled by their electric charges. Note that S must not be self-conjugated, implying $S^- \neq (S^+)^\dagger$ and $S^{2-} \neq (S^{2+})^\dagger$. In the second line, we reexpress the components with the tensor notation, where the sextuplet is represented by a totally symmetric rank-5 $SU(2)_L$ tensor S^{ijklm} with normalization factors ensuring

$$S_{ijklm}^\dagger S^{ijklm} = |S^{3+}|^2 + |S^{2+}|^2 + |S^+|^2 + |S^0|^2 + |S^-|^2 + |S^{2-}|^2. \quad (2)$$

The electrically neutral component S^0 can be divided into two real scalars ϕ^0 and a^0 ,

$$S^0 = \frac{1}{\sqrt{2}} (\phi^0 + ia^0). \quad (3)$$

The lighter real scalar is a DM candidate. For ensuring its stability, we impose a Z_2 symmetry $S \rightarrow -S$ to make the sextuplet inert.

The Lagrangian involving the sextuplet scalar reads

$$\mathcal{L} = (D^\mu S)_{ijklm}^\dagger (D_\mu S)^{ijklm} - V(S). \quad (4)$$

The covariant derivative of S is given by

$$(D_\mu S)^{ijklm} = \partial_\mu S^{ijklm} - 5ig(W_\mu)_n^i S^{njklm} - \frac{i}{2}g' B_\mu S^{ijklm}. \quad (5)$$

Here B_μ is the $U(1)_Y$ gauge field and $(W_\mu)_j^i \equiv W_\mu^a(\sigma^a)_{ij}/2$ is the $SU(2)_L$ gauge fields understood as a $(1, 1)$ tensor for the $SU(2)_L$ group, where σ^a denote the Pauli matrices. Thus, we have $(W_\mu)_1^1 = W_\mu^3/2 = -(W_\mu)_2^2$, $(W_\mu)_2^1 = W_\mu^+/\sqrt{2}$, and $(W_\mu)_1^2 = W_\mu^-/\sqrt{2}$. The electroweak gauge couplings of the sextuplet components are given in Appendix A.

We write down the Z_2 -invariant scalar potential involving S as

$$\begin{aligned} V(S) = & m_S^2 S_{ijklm}^\dagger S^{ijklm} + \lambda_1 H_i^\dagger S^{iklmn} S_{jklmn}^\dagger H^j + \lambda_2 H_i^\dagger S_{kmnpq}^\dagger S^{lmnpq} H^j \epsilon^{ik} \epsilon_{lj} \\ & + (\lambda_3 H_i^\dagger H_j^\dagger S^{iklmn} S^{jnpqs} \epsilon_{kp} \epsilon_{lq} \epsilon_{mr} \epsilon_{ns} + \text{H.c.}) \\ & + \text{quartic self-interaction terms of } S, \end{aligned} \quad (6)$$

where H^i is the SM Higgs doublet, and the rank-2 Levi-Civita symbol satisfies $\epsilon^{ij} = (i\sigma^2)_{ij} = -\epsilon_{ij}$. Note that $H_i^\dagger H^i S_{jklmn}^\dagger S^{ijklm} = H_i^\dagger S_{jklmn}^\dagger S^{iklmn} H^j + H_i^\dagger S_{kmnpq}^\dagger S^{lmnpq} H^j \epsilon^{ik} \epsilon_{lj}$, and hence a $H_i^\dagger H^i S_{jklmn}^\dagger S^{ijklm}$ term is not independent. As the quartic self-interaction terms of the sextuplet have no effects on the following discussions, we have not given their explicit expressions. If λ_3 is complex, say, $\lambda_3 = |\lambda_3|e^{i\alpha}$, we can always absorb the phase α by redefining the sextuplet scalar field as $e^{i\alpha/2}S$ to make λ_3 real and positive. Without loss of generality, we use $\lambda_3 \geq 0$ hereafter.

If the Z_2 symmetry $S \rightarrow -S$ is not respected, one may write down quartic terms like $H_i^\dagger S^{ijklm} S_{jknop}^\dagger S^{nopqr} \epsilon_{lq} \epsilon_{mr}$, which would lead to loop-induced decays of the DM candidate [23, 67, 68]. Therefore, such a Z_2 symmetry is not accidental, and we impose it by hand to stabilize the DM candidate.

After spontaneous breaking of the electroweak gauge symmetry, the λ_1 , λ_2 , and λ_3 terms in the unitary gauge become

$$\begin{aligned} V(S) \supset & \frac{\lambda_+}{4}(v+h)^2(|S^{3+}|^2 + |S^{2+}|^2 + |S^+|^2 + |S^0|^2 + |S^-|^2 + |S^{2-}|^2) \\ & + \frac{\lambda_-}{20}(v+h)^2(-5|S^{3+}|^2 - 3|S^{2+}|^2 - |S^+|^2 + |S^0|^2 + 3|S^-|^2 + 5|S^{2-}|^2) \\ & + \frac{\lambda_3}{10}(v+h)^2\left[2\sqrt{5}S^{2-}S^{2+} - 4\sqrt{2}S^-S^+ + 3(S^0)^2 + \text{H.c.}\right], \end{aligned} \quad (7)$$

where $\lambda_\pm \equiv \lambda_1 \pm \lambda_2$ and the VEV of the Higgs doublet is $v = (\sqrt{2}G_F)^{-1/2}$. Thus, the Higgs VEV contributes to the masses of the sextuplet components. The mass terms read

$$\begin{aligned} \mathcal{L}_{\text{mass}} = & -m_{S^{3\pm}}^2 |S^{3+}|^2 - \left((S^{2+})^\dagger \ S^{2-} \right) M_{2+}^2 \begin{pmatrix} S^{2+} \\ (S^{2-})^\dagger \end{pmatrix} - \left((S^+)^\dagger \ S^- \right) M_+^2 \begin{pmatrix} S^+ \\ (S^-)^\dagger \end{pmatrix} \\ & - \frac{1}{2}m_{\phi^0}^2 (\phi^0)^2 - \frac{1}{2}m_{a^0}^2 (a^0)^2. \end{aligned} \quad (8)$$

where the masses of the triply charged scalar $S^{3\pm}$ and the neutral scalars ϕ^0 and a^0 are given by

$$m_{S^{3\pm}}^2 = m_S^2 + \frac{1}{4}\lambda_+ v^2 - \frac{1}{4}\lambda_- v^2, \quad (9)$$

$$m_{\phi^0}^2 = m_S^2 + \frac{1}{4}\lambda_+ v^2 + \frac{1}{20}\lambda_- v^2 + \frac{3}{5}\lambda_3 v^2, \quad (10)$$

$$m_{a^0}^2 = m_S^2 + \frac{1}{4}\lambda_+ v^2 + \frac{1}{20}\lambda_- v^2 - \frac{3}{5}\lambda_3 v^2, \quad (11)$$

and the mass-squared matrices of the doubly and singly charged scalars are

$$M_{2+}^2 = \begin{pmatrix} m_S^2 + \frac{1}{4}\lambda_+ v^2 - \frac{3}{20}\lambda_- v^2 & \frac{\sqrt{5}}{5}\lambda_3 v^2 \\ \frac{\sqrt{5}}{5}\lambda_3 v^2 & m_S^2 + \frac{1}{4}\lambda_+ v^2 + \frac{1}{4}\lambda_- v^2 \end{pmatrix}, \quad (12)$$

$$M_+^2 = \begin{pmatrix} m_S^2 + \frac{1}{4}\lambda_+ v^2 - \frac{1}{20}\lambda_- v^2 & -\frac{2\sqrt{2}}{5}\lambda_3 v^2 \\ -\frac{2\sqrt{2}}{5}\lambda_3 v^2 & m_S^2 + \frac{1}{4}\lambda_+ v^2 + \frac{3}{20}\lambda_- v^2 \end{pmatrix}. \quad (13)$$

The gauge and mass eigenstates of the doubly and singly charged scalars are connected by rotations,

$$\begin{pmatrix} S^{2+} \\ (S^{2-})^\dagger \end{pmatrix} = R(\theta_{2+}) \begin{pmatrix} S_1^{2+} \\ S_2^{2+} \end{pmatrix}, \quad (14)$$

$$\begin{pmatrix} S^+ \\ (S^-)^\dagger \end{pmatrix} = R(\theta_+) \begin{pmatrix} S_1^+ \\ S_2^+ \end{pmatrix}, \quad (15)$$

with

$$R(\theta) = \begin{pmatrix} \cos \theta & -\sin \theta \\ \sin \theta & \cos \theta \end{pmatrix}. \quad (16)$$

These rotations diagonalize the mass-squared matrices, resulting in masses given by

$$m_{S_{1,2}^{2\pm}}^2 = m_S^2 + \frac{1}{4}\lambda_+ v^2 + \frac{1}{20}\lambda_- v^2 \mp \frac{1}{5}\sqrt{\lambda_-^2 + 5\lambda_3^2} v^2, \quad (17)$$

$$m_{S_{1,2}^\pm}^2 = m_S^2 + \frac{1}{4}\lambda_+ v^2 + \frac{1}{20}\lambda_- v^2 \mp \frac{1}{10}\sqrt{\lambda_-^2 + 32\lambda_3^2} v^2. \quad (18)$$

Here we adopt a mass hierarchy convention of $m_{S_1^{2\pm}}^2 \leq m_{S_2^{2\pm}}^2$ and $m_{S_1^\pm}^2 \leq m_{S_2^\pm}^2$. The rotation angles satisfy

$$\sin \theta_{2+} = \frac{-\sqrt{5/2}\lambda_3}{\sqrt{\lambda_-^2 + 5\lambda_3^2 + \lambda_- \sqrt{\lambda_-^2 + 5\lambda_3^2}}}, \quad (19)$$

$$\sin \theta_+ = \frac{4\lambda_3}{\sqrt{\lambda_-^2 + 32\lambda_3^2 + \lambda_- \sqrt{\lambda_-^2 + 32\lambda_3^2}}}. \quad (20)$$

Note that λ_+ equally contributes to all the scalar masses, and mass splittings are only induced by λ_- and λ_3 . Since we have adopted $\lambda_3 \geq 0$, a^0 is not heavier than ϕ^0 . In order to prevent any charged scalar lighter than a^0 , we should require $|\lambda_-| \leq 2\lambda_3$. In this case, a^0 is a viable DM candidate that cannot decay. The mass hierarchy of the dark sector scalars is

$$m_{a^0} \leq m_{S_1^\pm} \leq m_{S_1^{2\pm}} \leq m_{S_3^\pm} \leq m_{S_2^{2\pm}} \leq m_{S_2^\pm} \leq m_{\phi^0}. \quad (21)$$

Free parameters of the model are adopted to be

$$m_S, \quad \lambda_+, \quad \lambda_-, \quad \lambda_3. \quad (22)$$

The trilinear coupling between the Higgs boson h and the DM candidate a^0 is given by

$$\mathcal{L} \supset \frac{1}{2} \lambda_{haa} v h a^0 a^0, \quad (23)$$

$$\lambda_{haa} = -\frac{1}{2} \lambda_+ - \frac{1}{10} \lambda_- + \frac{6}{5} \lambda_3. \quad (24)$$

This coupling induces spin-independent (SI) a^0 scattering off nucleons in DM direct detection experiments. Making use of dimension-5 effective operators [69], we derive the a^0 -nucleon SI scattering cross section as

$$\sigma_{a^0 N}^{\text{SI}} = \frac{\lambda_{haa}^2 m_N^4 [2 + 7(f_u^N + f_d^N + f_s^N)]^2}{324\pi m_h^4 (m_{a^0} + m_N)^2}, \quad N = p, n, \quad (25)$$

where the form factors of nucleons $f_{u,d,s}^N$ can be found in Ref. [70].

Note that the condition

$$-\frac{1}{2} \lambda_+ - \frac{1}{10} \lambda_- + \frac{6}{5} \lambda_3 = 0 \quad (26)$$

corresponds to flat directions among the scalar couplings, where the Higgs VEV gives no contribution to the a^0 mass and the $h a^0 a^0$ coupling vanishes. In this case, a^0 -nucleon scattering is absent at tree level, and direct detection experiments would hardly constrain the model.

III. MASS SPLITTINGS AND SCALAR DECAYS

If electroweak gauge symmetry is strictly respected, the components of the sextuplet scalar must have a common mass m_S . Nonetheless, the VEV of the Higgs field breaks the degeneracy, leading nonzero mass splittings among the dark sector scalars. Figure 1(a) shows the mass splittings between the DM candidate a^0 and the other scalar bosons as functions of

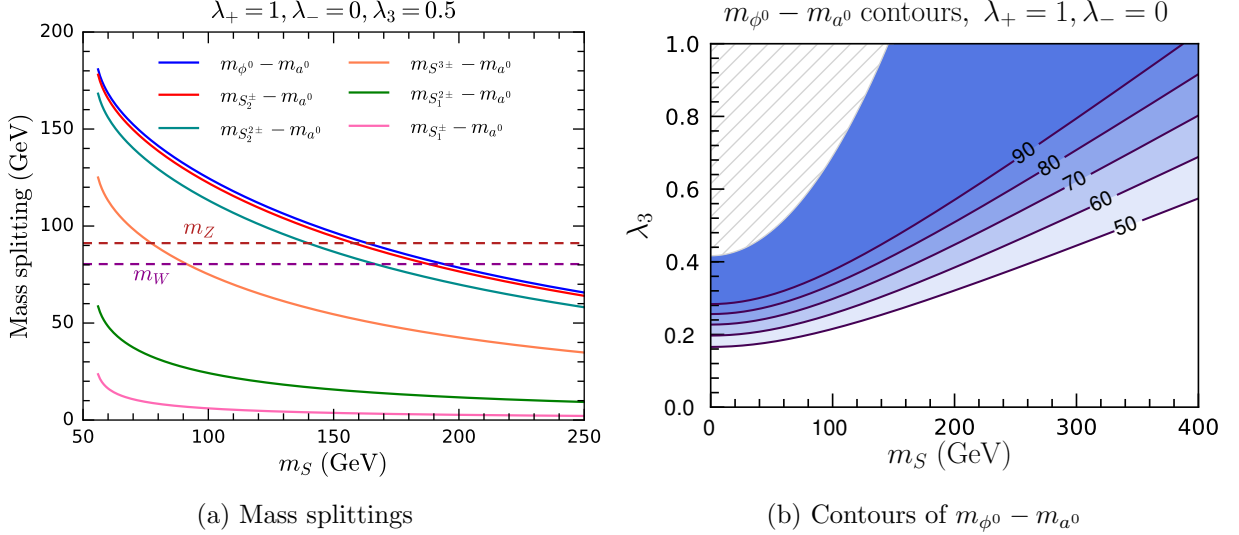


FIG. 1. Mass splittings among the dark sector scalars. (a) Mass splittings between a^0 and the other scalar bosons for $\lambda_+ = 1$, $\lambda_- = 0$, and $\lambda_3 = 0.5$. (b) Contours of the mass splitting in GeV between ϕ^0 and a^0 in the m_S - λ_3 plane for $\lambda_+ = 1$ and $\lambda_- = 0$.

m_S for $\lambda_+ = 1$, $\lambda_- = 0$, and $\lambda_3 = 0.5$. Note that m_S universally contributes to all the scalar masses. As m_S increases, the contributions to the masses from λ_- and λ_3 become relatively small, and hence the mass splittings decrease. In Fig. 1(a), we also indicate the masses of the W^\pm and Z bosons to show whether W/Z is on- or off-shell in the scalar decays.

The largest mass splitting among the scalars is $m_{\phi^0} - m_{a^0}$, whose contours in the m_S - λ_3 plane are demonstrated in Fig. 1(b) for $\lambda_+ = 1$ and $\lambda_- = 0$. We must ensure that the DM candidate a^0 has a physical mass, i.e., $m_a^2 > 0$, corresponding to $m_S^2 > 3\lambda_3 v^2/5 - \lambda_+ v^2/4 - \lambda_- v^2/20$. The hatched region in Fig. 1(b) is ruled out because it violates this condition. For $m_S \gtrsim 300$ GeV, the mass spectrum is rather compressed.

Dark sector scalars heavier than a^0 are unstable. They can decay into lighter states through the mediation of the weak gauge bosons W^\pm and Z and the Higgs boson h . The mediation particles could be either on or off shell, depending on the mass splittings. Important decay channels include $S^{3\pm}/S_i^{2\pm}/S_i^\pm \rightarrow S_1^{2\pm}/S_1^\pm/a^0 + W^{\pm(*)}$, $S_2^{2\pm}/S_2^\pm/\phi^0 \rightarrow S^{3\pm}/S_i^{2\pm}/S_i^\pm + W^{\mp(*)}$, $S_2^{2\pm}/S_2^\pm/\phi^0 \rightarrow S_1^{2\pm}/S_1^\pm/a^0 + Z^{(*)}$, and $S_2^{2\pm}/S_2^\pm \rightarrow S_1^{2\pm}/S_1^\pm + h^{(*)}$. The gauge and Higgs bosons subsequently convert to lighter SM particles. Typical 3-body decay diagrams are presented in Fig. 2. Because of the Z_2 symmetry, all decay chains finally end at the DM candidate a^0 . Typical mass splittings in this model are not large enough for an on-shell Higgs boson, and Higgs mediated decays into SM fermions are highly suppressed by the Yukawa couplings. Therefore, Higgs induced decays are commonly negligible.

For a scalar boson with 4-momentum p^μ and mass m decaying into three particles with 4-momenta k_1^μ , k_2^μ , and k_3^μ and masses m_1 , m_2 , and m_3 , the partial decay width can be

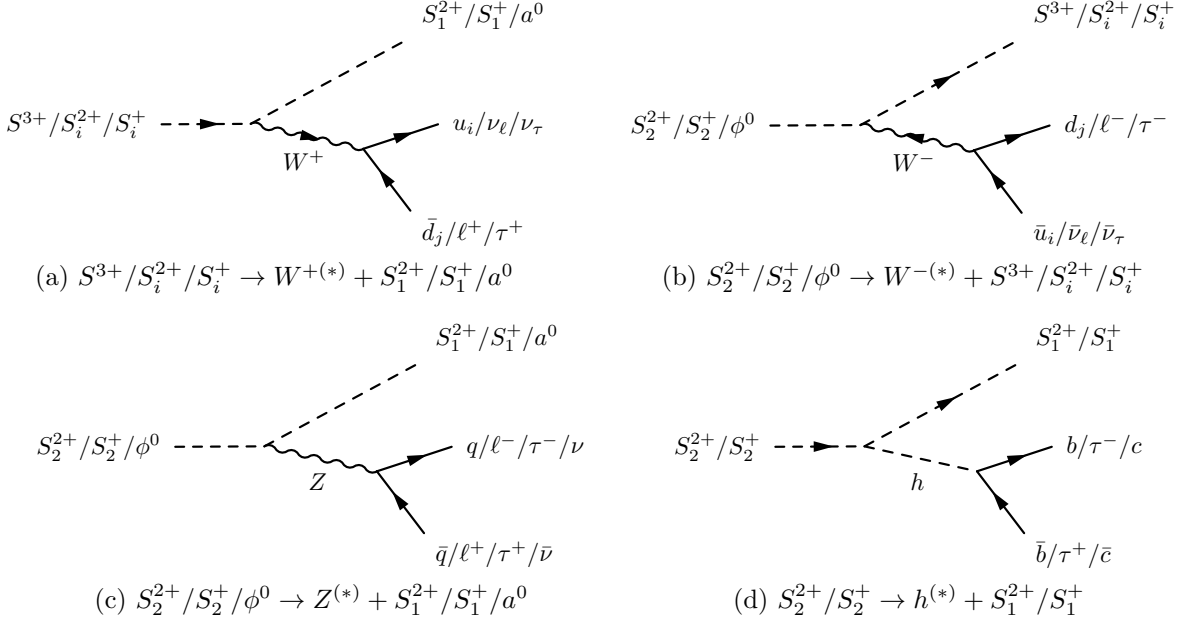


FIG. 2. Typical 3-body decay diagrams for $S^{3+}/S_i^{2+}/S_i^+ \rightarrow W^{+(*)} + S_1^{2+}/S_1^+/a^0$ (a), $S_2^{2+}/S_2^+/\phi^0 \rightarrow W^{-(*)} + S^{3+}/S_i^{2+}/S_i^+$ (b), $S_2^{2+}/S_2^+/\phi^0 \rightarrow Z^{(*)} + S_1^{2+}/S_1^+/a^0$ (c), and $S_2^{2+}/S_2^+ \rightarrow h^{(*)} + S_1^{2+}/S_1^+$ (d). Here $u_i = (u, c)$, $d_i = (d, s)$, $\ell = (e, \mu)$, and $q = (d, u, s, c, b)$.

expressed as [71]

$$\Gamma = \frac{1}{256\pi^3 m^3} \int_{s_{12}^{\min}}^{s_{12}^{\max}} ds_{12} \int_{s_{23}^{\min}}^{s_{23}^{\max}} ds_{23} |\mathcal{M}|^2, \quad (27)$$

where $|\mathcal{M}|^2$ is the invariant amplitude squared with summation over final state spins. The lower and upper limits of $s_{23} \equiv (k_2 + k_3)^2$ are given by

$$s_{23}^{\min} = (\tilde{E}_2 + \tilde{E}_3)^2 - \left(\sqrt{\tilde{E}_2^2 - m_2^2} + \sqrt{\tilde{E}_3^2 - m_3^2} \right)^2, \quad (28)$$

$$s_{23}^{\max} = (\tilde{E}_2 + \tilde{E}_3)^2 - \left(\sqrt{\tilde{E}_2^2 - m_2^2} - \sqrt{\tilde{E}_3^2 - m_3^2} \right)^2, \quad (29)$$

with

$$\tilde{E}_2 \equiv \frac{s_{12} - m_1^2 + m_2^2}{2\sqrt{s_{12}}}, \quad (30)$$

$$\tilde{E}_3 \equiv \frac{m^2 - s_{12} - m_3^2}{2\sqrt{s_{12}}}. \quad (31)$$

The lower and upper limits of $s_{12} \equiv (k_1 + k_2)^2$ are $s_{12}^{\min} = (m_1 + m_2)^2$ and $s_{12}^{\max} = (m - m_3)^2$.

For decay processes of the dark sector scalar bosons, we derive the tree-level $|\mathcal{M}|^2$ and calculate the partial widths and branching ratios utilizing the formulas above. For instance, the amplitude squared for the Z -mediated decay channel $\phi^0(p) \rightarrow a^0(k_1) + \bar{f}(k_2) + f(k_3)$,

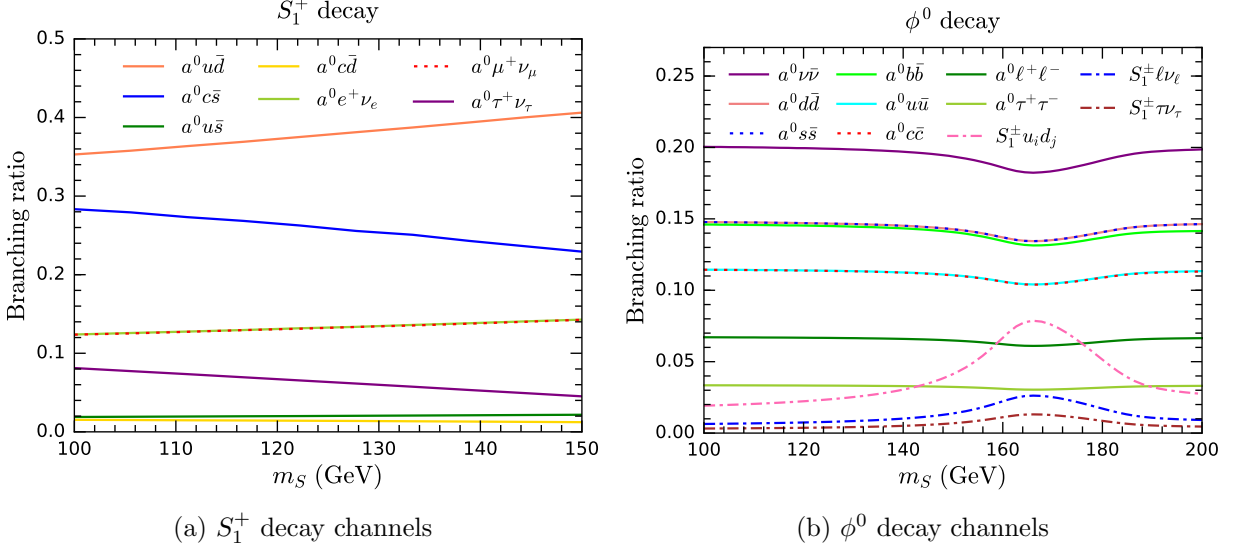


FIG. 3. Branching ratios of S_1^+ (a) and ϕ^0 (b) decay channels for $\lambda_+ = 1$, $\lambda_- = 0$, and $\lambda_3 = 0.5$.

where the 4-momenta are indicated between the parentheses, is obtained as

$$\begin{aligned}
|\mathcal{M}|^2 &= \frac{g^4}{2c_W^4 [(s_{23} - m_Z^2)^2 - m_Z^2 \Gamma_Z^2]} \\
&\times \left\{ (g_V^f)^2 [(s_{12} - m_f^2)(m_{\phi^0}^2 + m_{a^0}^2 + m_f^2 - s_{12} - s_{23}) - m_{\phi^0}^2 m_{a^0}^2] \right. \\
&\quad + (g_A^f)^2 [s_{12}(m_{\phi^0}^2 + m_{a^0}^2 - s_{12} - s_{23}) - m_{\phi^0}^2 m_{a^0}^2 + m_f^2(m_{\phi^0}^2 + m_{a^0}^2 + 2s_{12} - m_f^2) \\
&\quad \left. + m_f^2 m_Z^{-4} (m_{\phi^0}^2 - m_{a^0}^2)^2 (s_{23} - 2m_Z^2)] \right\}, \quad (32)
\end{aligned}$$

Here $c_W \equiv \cos \theta_W$ with $\theta_W = \tan^{-1}(g'/g)$ denoting the weak mixing angle. Γ_Z denotes the total width of Z , and g_V^f and g_A^f are the vector and axial-vector coupling coefficients of the SM fermion f to Z , respectively. On the other hand, the amplitude squared for the W -mediated decay channel $\phi^0(p) \rightarrow S_1^+(k_1) + \bar{d}_j(k_2) + u_i(k_3)$ with $u_i = (u, c)$ and $d_i = (d, s)$ is given by

$$\begin{aligned}
|\mathcal{M}|^2 &= \frac{g^4 |V_{ij}|^2 (3 \cos \theta_+ - 2\sqrt{2} \sin \theta_+)^2}{8 [(s_{23} - m_W^2)^2 + m_W^2 \Gamma_W^2]} \\
&\times \left\{ 4(m_{\phi^0}^2 - s_{12})(s_{12} - m_{S_1^\pm}^2) + (4s_{12} + s_{23})(m_{u_i}^2 + m_{d_j}^2) - 4s_{12}s_{23} - (m_{u_i}^2 + m_{d_j}^2)^2 \right. \\
&\quad - 2m_W^{-2} (m_{\phi^0}^2 - m_{S_1^\pm}^2) [(2s_{12} + s_{23})(m_{u_i}^2 - m_{d_j}^2) - 2m_{S_1^\pm}^2 m_{u_i}^2 + 2m_{\phi^0}^2 m_{d_j}^2 - m_{u_i}^4 + m_{d_j}^4] \\
&\quad \left. - m_W^{-4} (m_{\phi^0}^2 - m_{S_1^\pm}^2)^2 [(m_{u_i}^2 - m_{d_j}^2)^2 - s_{23}(m_{u_i}^2 + m_{d_j}^2)] \right\}, \quad (33)
\end{aligned}$$

where Γ_W is the total width of W and V_{ij} is the Cabibbo-Kobayashi-Maskawa matrix.

In Figs. 3(a) and 3(b), we show the branching ratios of the decay channels of S_1^+ and ϕ^0 , respectively. The parameters are fixed to be $\lambda_+ = 1$, $\lambda_- = 0$, and $\lambda_3 = 0.5$, as the same as

in Fig. 1(a).

The S_1^+ boson only has W -mediated decay channels. For the parameters adopted in Fig. 3(a), the W boson is always off shell. In the S_1^+ decay channels, the $S_1^+ \rightarrow a^0 u \bar{d}$ branching ratio $\mathcal{B}(S_1^+ \rightarrow a^0 u \bar{d})$ is the largest, while $\mathcal{B}(S_1^+ \rightarrow a^0 c \bar{s})$ is the second largest due to the suppression by the c and s quark masses. Because of the Cabibbo suppression, $\mathcal{B}(S_1^+ \rightarrow a^0 u \bar{s})$ and $\mathcal{B}(S_1^+ \rightarrow a^0 c \bar{d})$ are negligible. $\mathcal{B}(S_1^+ \rightarrow a^0 e^+ \nu_e)$ and $\mathcal{B}(S_1^+ \rightarrow a^0 \mu^+ \nu_\mu)$ are basically identical, reflecting the lepton universality, while $\mathcal{B}(S_1^+ \rightarrow a^0 \tau^+ \nu_\tau)$ is smaller, suppressed by the τ lepton mass. As m_S increases, the mass splitting between S_1^+ and a^0 decreases, leading to smaller phase spaces in the final states. Consequently, the $S_1^+ \rightarrow a^0 c \bar{s}$ and $S_1^+ \rightarrow a^0 \tau^+ \nu_\tau$ channels are more suppressed for larger m_S , resulting in larger $\mathcal{B}(S_1^+ \rightarrow a^0 u \bar{d})$ and $\mathcal{B}(S_1^+ \rightarrow a^0 \ell^+ \nu_\ell)$, where $\ell = e, \mu$.

Figure 3(b) demonstrates the Z -mediated ϕ^0 decay channels into a^0 as well as the W -mediated channels into S_1^\pm . Because of the tiny mass splitting between ϕ^0 and S_2^\pm , the ϕ^0 decay channels into S_2^\pm are negligible and not shown in the plot. In the Z -mediated channels, $\mathcal{B}(\phi^0 \rightarrow a^0 \nu \bar{\nu})$ is as large as $\sim 20\%$. The ϕ^0 decay into a down-type (up-type) quark pair has a branching ratio $\sim 15\%$ ($\sim 11\%$), while the ϕ^0 decay into a charged lepton pair has a branching ratio $\sim 3\%$.

For a region around $m_S \sim 165$ GeV in Fig. 3(b), the Z -mediated channels commonly decrease; in contrast, the W -mediated channels commonly increase. This can be understood by comparing with the mass splittings shown in Fig. 1(a). For $m_S \lesssim 160$ GeV, we have $m_{\phi^0} - m_{a^0} \gtrsim m_Z$ and the on-shell Z and W bosons dominate over the phase spaces. In this case, the ϕ^0 decays can be treated as 2-body decays $\phi^0 \rightarrow a^0 Z$ and $\phi^0 \rightarrow S_1^\pm W^\mp$, where the weak gauge bosons subsequently decay into SM fermions. For $m_S \gtrsim 160$ GeV, however, the Z boson becomes off shell. Thus, the Z -mediated channels are suppressed by the phase spaces of 3-body final states. A similar suppression on the W -mediated channels happens later, at $m_S \gtrsim 185$ GeV, where the behaviors of the two types of channels are gradually restored.

IV. SEARCHES AT pp COLLIDERS

High energy colliders are primary tools for finding new particles. Currently, the highest center-of-mass energy in pp collisions is $\sqrt{s} = 13$ TeV, achieved by the LHC, which will be soon upgraded to $\sqrt{s} = 14$ TeV. Moreover, a future pp collider with $\sqrt{s} \sim 100$ TeV would provide great opportunities for discovering the new scalar bosons in the inert sextuplet scalar model.

The dark sector scalars can be directly produced in pairs at pp colliders through electroweak gauge interactions. The inclusive production processes can be represented as $pp \rightarrow S_i S_j + \text{jets}$ with $S_i = (a^0, \phi^0, S_1^\pm, S_2^\pm, S_1^{2\pm}, S_2^{2\pm}, S^{3\pm})$. The corresponding Feynman diagrams at parton level are demonstrated in Fig. 4. The inclusive production cross section

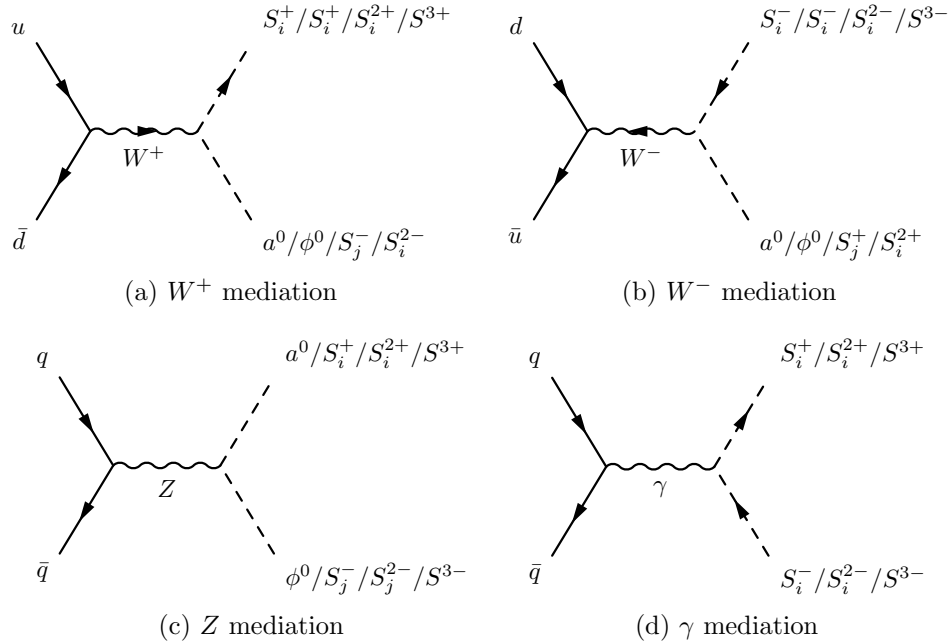


FIG. 4. Typical Feynman diagrams for the scalar pair production at pp colliders, including W^+ -mediated $u+\bar{d} \rightarrow S_i^+/S_i^+/S_i^{2+}/S^{3+}+a^0/\phi^0/S_j^-/S_i^{2-}$ (a), W^- -mediated $d+\bar{u} \rightarrow S_i^-/S_i^-/S_i^{2-}/S^{3-}+a^0/\phi^0/S_j^+/S_i^{2+}$ (b), Z -mediated $q+\bar{q} \rightarrow a^0/S_i^+/S_i^{2+}/S^{3+}+\phi^0/S_j^-/S_j^{2-}/S^{3-}$ (c), and γ -mediated $q+\bar{q} \rightarrow S_i^+/S_i^{2+}/S^{3+}+S_i^-/S_i^{2-}/S^{3-}$ (d).

as a function of m_S is shown in Fig. 5 for $\lambda_+ = \lambda_- = \lambda_3 = 0$, which implies that all dark sector scalars have a common mass m_S . For $m_S \sim 200$ GeV, the cross section is ~ 1 pb at $\sqrt{s} = 13$ TeV, and increases to ~ 30 pb at $\sqrt{s} = 100$ TeV. For $m_S \gtrsim 700$ GeV, the cross section increases by more than two orders of magnitude when \sqrt{s} is promoted from 13 TeV to 100 TeV.

Since the only stable scalar is the DM candidate a^0 , all other scalars finally decay into a^0 , associated with visible particles. General detectors at the LHC and future pp colliders cannot probe a^0 , which would give rise to a missing transverse momentum \cancel{p}_T in the final state. The missing transverse energy is defined as $\cancel{E}_T \equiv |\cancel{p}_T|$, characterizing the energy amount of the particles that do not recorded by the detector. Therefore, a large \cancel{E}_T is an important imprint for a^0 . According to other information from the associating visible particles, we can utilize different channels to search for the dark sector scalars. In the following subsections, we separately discuss the monojet + \cancel{E}_T and soft-dilepton + jets + \cancel{E}_T search channels.

We will investigate the current LHC constraints on the inert sextuplet scalar model by reinterpreting the experimental analyses at $\sqrt{s} = 13$ TeV and study the future sensitivity at a 100 TeV pp collider. For this purpose, we need to generate Monte Carlo simulation samples for the signals and relevant backgrounds. The inert sextuplet model is implemented by `FeynRules 2` [72], which reads off the Lagrangian we defined and outputs the Feynman rules for Monte Carlo tools. Moreover, `MadGraph5_aMG@NLO 2` [73] is utilized to automatically

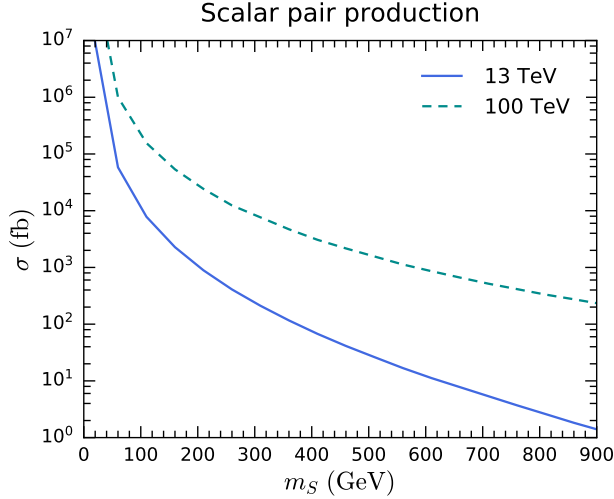


FIG. 5. Production cross sections as functions of m_S for $pp \rightarrow S_i S_j + \text{jets}$ with $S_i = (a^0, \phi^0, S_1^\pm, S_2^\pm, S_1^{2\pm}, S_2^{2\pm}, S^{3\pm})$ at $\sqrt{s} = 13$ TeV and 100 TeV. The couplings are fixed as $\lambda_+ = \lambda_- = \lambda_3 = 0$.

generate Feynman diagrams, calculate matrix elements, perform phase space integrations, and generate parton-level event samples. Furthermore, we use `PYTHIA 8` [74] to carry out parton shower, hadronization, and particle decays. The MLM matching scheme [75] is adopted for merging matrix element and parton shower calculations. Finally, `Delphes 3` [76] is used for a fast, simplified detector simulation with a parametrization of the ATLAS detector.

A. Monojet + \cancel{E}_T channel

From the analysis in Sec. III as well as Fig. 1, we know that the mass splittings among the dark sector scalars are quite small for small scalar couplings and/or large m_S . Therefore, in a large portion of the parameter space, the visible products from the scalar decays are quite soft. It is possible to utilize soft leptons (electrons and muons) for probing the signal, and we will discuss this possibility in the next subsection. In the present subsection, we choose to neglect the soft particles and consider at least one energetic jet originated from initial state radiation to recoil against the scalar pair for achieving a large \cancel{E}_T . Isolated leptons are further vetoed to give a clear signature. This leads to the monojet + \cancel{E}_T search channel, which has been widely used at the LHC for DM searches [41, 55, 77–81].

The primary background in the monojet + \cancel{E}_T channel is $Z(\rightarrow \nu\bar{\nu}) + \text{jets}$, where the neutrinos from Z decays cannot be detected and also lead to missing transverse energy. The subdominant background is $W(\rightarrow \ell\nu) + \text{jets}$, where the charged lepton ℓ could either fall outside of the detector acceptance or be combined into a jet [77]. Minor backgrounds include small fractions of $Z/\gamma^*(\rightarrow \ell^+\ell^-) + \text{jets}$, multijet, $t\bar{t} + \text{jets}$, single top, diboson (WW, WZ, ZZ)

TABLE I. Signal regions in the ATLAS monojet + \cancel{E}_T analysis at $\sqrt{s} = 13$ TeV [83]. σ_{vis}^{95} is the observed 95% C.L. upper limit on the visible cross section σ_{vis} .

Signal regions	IM1	IM2	IM3	IM4	IM5	IM6	IM7	IM8
\cancel{E}_T (GeV)	> 250	> 300	> 350	> 400	> 500	> 600	> 700	> 800
σ_{vis}^{95} (fb)	531	330	188	93	43	19	7.7	4.9

processes [82]. The multijet background can be efficiently reduced by requiring a sufficient large azimuthal angle $\Delta\phi(j, \mathbf{p}_T)$ between \mathbf{p}_T and each reconstructed jet j .

1. LHC constraint

Firstly, we utilize the monojet + \cancel{E}_T analysis from the ATLAS experiment with an integrated luminosity of 36.1 fb^{-1} at $\sqrt{s} = 13$ TeV [83] to evaluate the monojet constraint on the model. In the ATLAS analysis, reconstructed jets are required to have $p_T > 30$ GeV and $|\eta| < 2.8$, while reconstructed isolated electrons (muons) should have $p_T > 20$ (10) GeV and $|\eta| < 2.47$ (2.5). Then the following selection cuts are applied for increasing the signal significance: (a) $\cancel{E}_T > 250$ GeV; (b) a leading jet with $p_T > 250$ GeV and $|\eta| < 2.4$; (c) no more than four jets; (d) $\Delta\phi(j, \mathbf{p}_T) > 0.4$; (e) no isolated electron or muon.

Moreover, various signal regions are defined according to further cuts on \cancel{E}_T , aiming at various models and different DM particle masses. In each signal region, the ATLAS collaboration derives the observed upper limit at 95% confidence level (C.L.) on the visible cross section σ_{vis} , which is defined as the product of production cross section, acceptance, and efficiency. Here we choose several inclusive signal regions tabulated in Table I. Based on simulation, we estimate the visible cross section in these signal regions for the inert sextuplet model and derive experimental bounds.

The 95% C.L. exclusion region in the m_S - λ_3 plane for $\lambda_+ = \lambda_- = 2\lambda_3$ with the eight signal regions combined are shown in Fig. 6. Note that the parameter relation $\lambda_+ = \lambda_- = 2\lambda_3$ satisfies the condition (26), and hence direct detection experiments give no constraint. Furthermore, this relation leads to degenerate mass spectra at tree level with

$$m_{a^0} = m_{S_1^\pm} = m_{S_1^{2\pm}} = m_{S^{3\pm}} < m_{S_2^{2\pm}} = m_{S_2^\pm} = m_{\phi^0}. \quad (34)$$

Although electroweak loop corrections break the degeneracy and slightly lift up the masses of S_1^\pm , $S_1^{2\pm}$, and $S^{3\pm}$ [8], the mass splittings between these scalar bosons and a^0 are too small to induce hard visible particles that can be triggered in monojet searches. Therefore, in this case these scalars also contribute to \cancel{E}_T , and one would expect a fairly well sensitivity in the monojet channel. Nevertheless, Fig. 6 shows that the 13 TeV monojet search only explore a region up to $m_S \sim 85$ GeV.

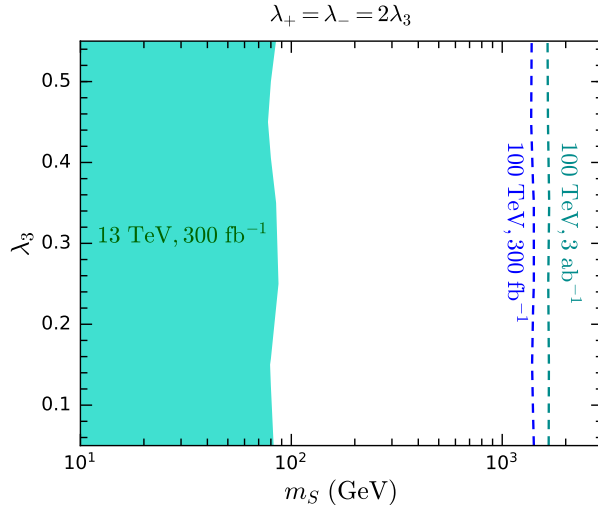


FIG. 6. Current constraint and future sensitivity of the monojet + \cancel{E}_T channel in the m_S - λ_3 plane for $\lambda_+ = \lambda_- = 2\lambda_3$. The turquoise region is excluded at 95% C.L. by the 13 TeV ATLAS monojet + \cancel{E}_T search with a dataset of 36.1 fb^{-1} [83]. The blue and purple dashed lines denote the expected 95% C.L. exclusion limits at a 100 TeV pp collider with integrated luminosities 300 fb^{-1} and 3 ab^{-1} , respectively.

2. 100 TeV pp collider sensitivity

Since the monojet + \cancel{E}_T search at the LHC does not explore the model well, we turn to study this channel at a 100 TeV pp collider and estimate the improvement of the sensitivity. We simulate signal and background event samples for pp collisions at $\sqrt{s} = 100 \text{ TeV}$. Only two dominant SM backgrounds, $Z(\rightarrow \nu\bar{\nu}) + \text{jets}$ and $W(\rightarrow \ell\nu) + \text{jets}$, are considered. Then we require reconstructed jets to have $p_T > 80 \text{ GeV}$ and $|\eta| < 2.8$, and reconstructed electrons (muons) to have $p_T > 20$ (10) GeV and $|\eta| < 2.47$ (2.5). Similar to the 13 TeV search, the following selection cuts are applied to the simulation samples.

- *Cut 1.*—A leading jet with $p_T > 1.5 \text{ TeV}$ and $|\eta| < 2.4$.
- *Cut 2.*—No more than four reconstructed jets.
- *Cut 3.*— $\Delta\phi(j, \cancel{p}_T) > 0.4$.
- *Cut 4.*—No reconstructed electron or muon.
- *Cut 5.*— $\cancel{E}_T > 1.6 \text{ TeV}$.

As illuminating examples, we consider four benchmark points (BMPs), whose detailed information is listed in Table II. All the four BMPs satisfy the condition (26), leading to $m_{a^0} = m_S$, and there is no constraint from direct detection experiments. The mass spectra in these BMPs have various degrees of compression, which can be represented by the largest mass splitting $m_{\phi^0} - m_{a^0}$.

TABLE II. Information of four BMPs.

	BMP1	BMP2	BMP3	BMP4
λ_+	0.84	0.41	0.55	0.345
λ_-	0.6	0.35	0.25	0.075
λ_3	0.4	0.2	0.25	0.15
m_S (GeV)	250	200	300	300
m_{a^0}, m_{ϕ^0} (GeV)	250, 302.65	200, 233.56	300, 328.92	300, 317.67
$m_{S_1^\pm}, m_{S_2^\pm}$ (GeV)	250.72, 302.06	200.24, 233.35	300.64, 328.33	300.49, 317.21
$m_{S_1^{2\pm}}, m_{S_2^{2\pm}}$ (GeV)	252.96, 300.18	200.97, 232.72	302.77, 326.37	302.14, 315.63
$m_{S^{3\pm}}$ (GeV)	257.17	202.26	307.48	306.74
$m_{\phi^0} - m_{a^0}$ (GeV)	52.65	33.56	28.92	17.67
$\text{BR}(\phi^0 \rightarrow a^0 \ell^+ \ell^-)$	3.37%	3.00%	4.64%	6.21%
$\text{BR}(S_2^\pm \rightarrow S_1^\pm \ell^+ \ell^-)$	2.99%	2.63%	4.16%	5.62%
$\text{BR}(S_2^{2\pm} \rightarrow S_1^{2\pm} \ell^+ \ell^-)$	2.51%	2.17%	7.21%	7.23%
S	0.0448	0.0426	0.0142	0.00440
T	-0.0222	-0.00483	-0.0113	-0.00525
U	-0.00589	-0.00208	-0.00226	-0.00108

TABLE III. Visible cross section σ_{vis} in fb for the backgrounds and signal BMPs after each cut in the monojet + \cancel{E}_T channel at $\sqrt{s} = 100$ TeV. The signal significance \mathcal{S} corresponds to integrated luminosity 3 ab^{-1} for $\beta = 1\%$ and $\gamma = 10\%$.

	$W \rightarrow \ell\nu$	$Z \rightarrow \nu\bar{\nu}$	BMP1		BMP2		BMP3		BMP4	
	σ_{vis}	σ_{vis}	σ_{vis}	\mathcal{S}	σ_{vis}	\mathcal{S}	σ_{vis}	\mathcal{S}	σ_{vis}	\mathcal{S}
Cut 1	4620	1135	53.5	0.926	65.7	1.13	45.3	0.784	44.1	0.763
Cut 2	3652	922	46.2	1.00	56.1	1.22	40.3	0.878	39.8	0.867
Cut 3	1913	537	31.4	1.27	37.1	1.50	28.4	1.15	29.3	1.19
Cut 4	1168	537	29.6	1.71	35.1	2.02	26.3	1.52	27.5	1.59
Cut 5	48.7	111	16.8	7.21	19.7	7.73	16.1	7.07	17.1	7.26

In order to estimate the sensitivity at a future pp collider, we define the signal significance as [84]

$$\mathcal{S} = \frac{N_S}{\sqrt{N_B + (\beta N_B)^2 + (\gamma N_S)^2}}, \quad (35)$$

where N_S (N_B) is the number of signal (total background) events. β and γ represent the fractions of systematic uncertainties on N_B and on N_S , respectively. For the monojet channel at $\sqrt{s} = 100$ TeV, we assume $\beta = 1\%$ and $\gamma = 10\%$.

In Table III, we list the visible cross sections for the backgrounds and the four signal BMPs after each cut applied, as well as the signal significances of the BMPs. The veto on

leptons in cut 4 reduces $\sim 39\%$ of the $W(\rightarrow \ell\nu) + \text{jets}$ background, since it often induces a hard lepton. The signal significances of the four BMPs remarkably increase after applying cut 5, reaching above 7. Overall, we find that these cuts efficiently suppress the backgrounds and increase \mathcal{S} .

Now we define four signal regions by separately requiring $\cancel{E}_T > 1.6, 1.8, 2, 2.5$ TeV. The expected exclusion limit at 95% C.L. combining these signal regions in the monojet channel with $\sqrt{s} = 100$ TeV has been shown in Fig. 6 for $\lambda_+ = \lambda_- = 2\lambda_3$. We find that the 100 TeV monojet search could explore the parameter space up to $m_S \sim 1.4$ (1.65) TeV for an integrated luminosity of 300 fb^{-1} (3 ab^{-1}).

B. Soft-dilepton + jets + \cancel{E}_T channel

As discussed above, the mass spectrum of the inert sextuplet scalar model is typically compressed. Consequently, leptons (electrons and muons) from off-shell Z and W bosons in the scalar decays are usually quite soft. Nevertheless, it is still possible to make use of such soft leptons for searching for dark sector scalars [85–89]. We will focus on a pair of same-flavor opposite-sign (SFOS) leptons (either e^+e^- or $\mu^+\mu^-$) from off-shell Z decays, because they are rather unique for signal-background discrimination. The relevant scalar decay processes are $S_2^{2+} \rightarrow S_1^{2+} + Z^*(\rightarrow \ell^+\ell^-)$, $S_2^+ \rightarrow S_1^+ + Z^*(\rightarrow \ell^+\ell^-)$, and $\phi^0 \rightarrow a^0 + Z^*(\rightarrow \ell^+\ell^-)$, whose Feynman diagrams are shown in Fig. 2(c) and branching ratios are exemplified in Table II. Some additional jets are allowed for keeping more signal events. In particular, one hard jet recoiling against the dark sector scalar pair is helpful for inducing a larger \cancel{E}_T and making the soft leptons more easy to be triggered. Thus, the search channel we would like to study is soft-dilepton + jets + \cancel{E}_T .

The important SM backgrounds in this channel are $t\bar{t} + \text{jets}$, $tW + \text{jets}$, $VV + \text{jets}$ ($V = W^\pm, Z$), and $\tau^+\tau^- + \text{jets}$. The top quark exclusively decays via the weak process $t \rightarrow bW$. If the two W bosons from a $t\bar{t}$ pair decay leptonically, the final state would contain a pair of leptons associated with undetected neutrinos, mimicking the signal. The $tW + \text{jets}$ background has a similar feature, but its production rate is lower. Nonetheless, a veto on b -tagged jets would be able to efficiently suppress both the $t\bar{t} + \text{jets}$ and $tW + \text{jets}$ backgrounds. Moreover, the $VV + \text{jets}$ and $\tau^+\tau^- + \text{jets}$ backgrounds can contribute to the soft-dilepton + jets + \cancel{E}_T final state when the decays of the W/Z bosons or the taus produce a SFOS lepton pair.

Utilizing the information from the SFOS lepton pair and \cancel{p}_T , we can construct the $m_{\tau\tau}$ variable [88–91] for reducing the $\tau^+\tau^- + \text{jets}$ background. When a tau pair recoils against an energetic jet, the taus are highly boosted and their decay products would be nearly parallel. In this case, for leptonic tau decays, the momentum of a daughter neutrino is basically collinear to the momentum of the corresponding daughter lepton. Thus, the 4-momentum of a neutrino ν_i can be expressed as $p_{\nu_i}^\mu = \xi_i p_{\ell_i}^\mu$, where $p_{\ell_i}^\mu$ is the 4-momentum of the related

lepton ℓ_i and the lepton mass has been neglected. Therefore, the total missing transverse momentum becomes $\mathbf{p}_T = \xi_1 \mathbf{p}_T^{\ell_1} + \xi_2 \mathbf{p}_T^{\ell_2}$. By solving the two equations provided by this relation, we obtain the values of ξ_1 and ξ_2 for given \mathbf{p}_T , $\mathbf{p}_T^{\ell_1}$, and $\mathbf{p}_T^{\ell_2}$. Since the 4-momentum of each tau is $p_{\tau_i}^\mu = p_{\ell_i}^\mu + p_{\nu_i}^\mu = (1 + \xi_i)p_{\ell_i}^\mu$, the invariant mass squared of the $\tau^+\tau^-$ pair can be expressed as $m_{\tau\tau}^2 = 2(1 + \xi_1)(1 + \xi_2)p_{\ell_1} \cdot p_{\ell_2}$ after neglecting the tau mass. The $m_{\tau\tau}$ variable is defined as $m_{\tau\tau} \equiv \text{sign}(m_{\tau\tau}^2)\sqrt{|m_{\tau\tau}^2|}$. By this definition, $m_{\tau\tau}$ can be either positive or negative in practice. Nonetheless, $m_{\tau\tau}$ approximates the true invariant mass of a highly boosted $\tau^+\tau^-$ pair with leptonically decays. We will see later that a veto on events with $0 < m_{\tau\tau} < 200$ GeV is helpful for suppressing both the $\tau^+\tau^- + \text{jets}$ and $VV + \text{jets}$ backgrounds at a 100 TeV pp collider.

1. LHC constraint

The soft-dilepton + jets + \cancel{E}_T channel has been used in the ATLAS search for electroweak production of supersymmetric particles with compressed mass spectra at $\sqrt{s} = 13$ TeV with a dataset of 36.1 fb^{-1} [91]. We make use of the related search results to constrain the inert sextuplet model.

In the ATLAS search, reconstructed electrons (muons) are required to have $p_T > 4.5$ (4) GeV and $|\eta| < 2.47$ (2.5), while reconstructed jets should have $p_T > 20$ GeV and $|\eta| < 4.5$. The following selection conditions are further applied.

- A SFOS lepton pair (e^+e^- or $\mu^+\mu^-$) and no other leptons. The leading lepton ℓ_1 has $p_T^{\ell_1} > 5$ GeV. The subleading lepton ℓ_2 has $p_T^{\ell_2} > 4.5$ (4) GeV if it is an electron (muon). The angular distance $\Delta R \equiv \sqrt{\Delta\phi^2 + \Delta\eta^2}$ between the two leptons satisfies $\Delta R_{\ell\ell} \in (0.05, 2)$. The invariant mass of the two leptons satisfies $m_{\ell\ell} \in [1, 3) \cup (3.2, 60]$ GeV, where the $[3, 3.2]$ GeV window is excluded for evading contributions from J/ψ decays.
- At least one jet but no b -tagged jet. Each jet j satisfies $\Delta\phi(j, \mathbf{p}_T) > 0.4$. The leading jet j_1 satisfies $p_T^{j_1} > 100$ GeV and $\Delta\phi(j_1, \mathbf{p}_T) > 2$.
- $\cancel{E}_T > 200$ GeV, $m_T^{\ell_1} < 70$ GeV, and $\cancel{E}_T/H_T^{\text{lep}} > \max(5, 15 - 2m_{\ell\ell}/\text{GeV})$, where $m_T^{\ell_1} \equiv \sqrt{2(E_T^{\ell_1} \cancel{E}_T - \mathbf{p}_T^{\ell_1} \cdot \mathbf{p}_T)}$ and $H_T^{\text{lep}} \equiv p_T^{\ell_1} + p_T^{\ell_2}$. Veto on events with $m_{\tau\tau} \in [0, 160]$ GeV.

Then the ATLAS collaboration defines seven signal regions with different inclusive bins of $m_{\ell\ell}$, and obtains the 95% C.L. observed upper limit on the visible cross section, as listed in Table IV.

Combining these seven signal regions, we derive the 95% C.L. exclusion region in the m_S - λ_3 plane for $\lambda_+ = \lambda_- = 2\lambda_3$, as presented in Fig. 7. We find that the soft-dilepton + jets + \cancel{E}_T channel at the current LHC is more sensitive than the monojet + \cancel{E}_T channel, excluding a region up to $m_S \sim 210$ GeV.

TABLE IV. Signal regions in the ATLAS soft-dilepton + jets + \cancel{E}_T analysis at $\sqrt{s} = 13$ TeV [91]. σ_{vis}^{95} denotes the observed 95% C.L. upper limit on the visible cross section σ_{vis} .

$m_{\ell\ell}/\text{GeV} \in$	[1, 3]	[1, 5]	[1, 10]	[1, 20]	[1, 30]	[1, 40]	[1, 60]
σ_{vis}^{95} (fb)	0.1	0.18	0.34	0.61	0.59	0.72	0.80

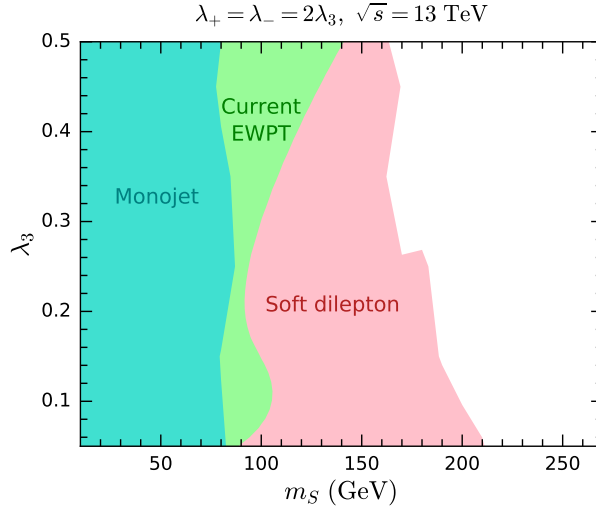


FIG. 7. Current constraints in the m_S - λ_3 plane for $\lambda_+ = \lambda_- = 2\lambda_3$. The pink (turquoise) region is excluded at 95% C.L. by the ATLAS soft-dilepton + jets + \cancel{E}_T analysis [91] (monojet + \cancel{E}_T analysis [83]) at $\sqrt{s} = 13$ TeV with a dataset of 36.1 fb^{-1} . The light green region is excluded at 95% C.L. by the global fit in the current EWPT from the Gfitter Group [92] (see Sec. V).

2. 100 TeV pp collider sensitivity

Now we investigate the sensitivity of the soft-dilepton + jets + \cancel{E}_T channel at a 100 TeV pp collider. We require reconstructed leptons to have $p_T > 10$ GeV and $|\eta| < 2.5$, and reconstructed jets to have $p_T > 40$ GeV and $|\eta| < 4.5$. We apply the following selection cuts to the simulation samples.

- *Cut 1.*—A SFOS lepton pair and no other leptons; $\cancel{E}_T > 300$ GeV; at least one jet; $\Delta\phi(j, \mathbf{p}_T) > 0.4$ for any jet j ; $p_T^{j_1} > 240$ GeV and $\Delta\phi(j_1, \mathbf{p}_T) > 2$ for the leading jet j_1 .
- *Cut 2.*— $0.05 < \Delta R_{\ell\ell} < 2$.
- *Cut 3.*— $m_{\tau\tau} < 0$ or $m_{\tau\tau} > 200$ GeV.
- *Cut 4.*—No b -tagged jet.
- *Cut 5.*— $m_{\ell\ell} \in [1, 3) \cup (3.2, 70]$ GeV.

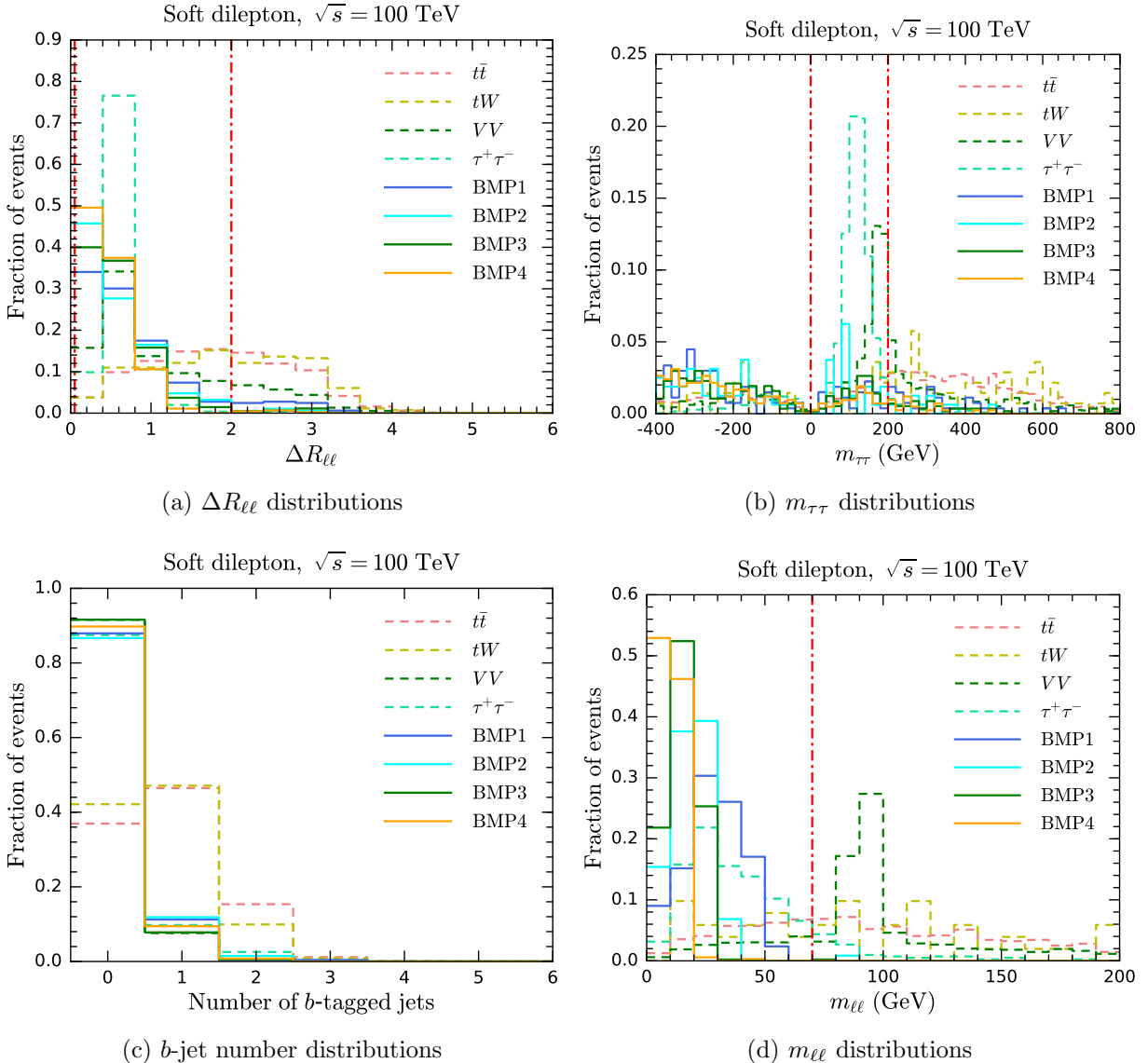


FIG. 8. Fractions of background and signal events binned in $\Delta R_{\ell\ell}$ after cut 1 (a), in $m_{\tau\tau}$ after cut 2 (b), in the number of b -tagged jets after cut 3 (c), and in $m_{\ell\ell}$ after cut 4 (d) for the soft-dilepton + jets + \cancel{E}_T channel at $\sqrt{s} = 100$ TeV. The red dot-dashed lines indicate the cut thresholds.

We find that the $m_{T}^{\ell_1}$ and $\cancel{E}_T/H_T^{\text{lep}}$ cuts used in the 13 TeV ATLAS analysis are not helpful for the inert sextuplet model, so these two cuts are abandoned for $\sqrt{s} = 100$ TeV.

In order to justify these cut conditions, we demonstrate the distributions of backgrounds and signal BMPs in Fig. 8. These distributions are expressed as the fractions of events binned in kinematic variables. Moreover, the visible cross sections and the BMP signal significances are tabulated in Table V. For the soft-dilepton + jets + \cancel{E}_T channel at $\sqrt{s} = 100$ TeV, we assume the fractions of the systematic uncertainties to be $\beta = 1\%$ and $\gamma = 10\%$.

Firstly, Fig. 8(a) shows the $\Delta R_{\ell\ell}$ distributions after applying cut 1. As we can see, the

TABLE V. Visible cross section σ_{vis} in fb for the backgrounds and signal BMPs after the cuts and for the signal regions in the soft-dilepton + jets + \cancel{E}_T channel at $\sqrt{s} = 100$ TeV. The signal significance \mathcal{S} corresponds to integrated luminosity 3 ab^{-1} for $\beta = 1\%$ and $\gamma = 10\%$.

	$t\bar{t}$	tW	VV	$\tau^+\tau^-$	BMP1		BMP2		BMP3		BMP4	
	σ_{vis}	σ_{vis}	σ_{vis}	σ_{vis}	σ_{vis}	\mathcal{S}	σ_{vis}	\mathcal{S}	σ_{vis}	\mathcal{S}	σ_{vis}	\mathcal{S}
Cut 1	2026	354	374	111	7.97	0.278	8.78	0.306	10.1	0.352	7.75	0.270
Cut 2	1140	186	303	111	6.55	0.376	7.47	0.429	9.30	0.534	7.13	0.409
Cut 3	970	162	175	20.7	5.87	0.441	6.30	0.474	8.15	0.611	6.50	0.488
Cut 4	358	68.3	160	18.1	5.16	0.847	5.46	0.897	7.46	1.22	5.84	0.957
Cut 5	119	25.5	29.1	15.7	5.16	2.61	5.37	2.71	7.41	3.62	5.82	2.91
SR-60	94.8	22.8	22.6	14.6	5.16	3.13	5.37	3.25	7.41	4.28	5.82	3.49
SR-40	51.9	13.4	12.9	10.2	4.15	4.19	5.37	5.12	7.41	6.35	5.80	5.41
SR-20	16.8	6.70	3.98	3.43	1.25	3.58	2.85	6.59	5.51	8.61	5.77	8.71

$t\bar{t}$ + jets and tW + jets backgrounds tend to have much larger $R_{\ell\ell}$ than the BMPs and the other backgrounds. A part of the VV + jets background exhibits a similar behavior. This is because the two leptons come from decays of different particles in $t\bar{t}$, tW , and W^+W^- and prefer to fly in opposite directions. For the BMPs and the VV + jets and $\tau^+\tau^-$ + jets backgrounds, the SFOS lepton pair could come from an on- or off-shell Z boson, which is sufficiently boosted due to the requirements of $\cancel{E}_T > 300$ GeV and $p_T^{\cancel{E}_T} > 240$ GeV in cut 1, and give small $\Delta R_{\ell\ell}$. Thus, the $\Delta R_{\ell\ell}$ cut is rather useful for suppressing the $t\bar{t}$ + jets and tW + jets backgrounds, and also reduces the VV + jets background. From Table V, we find that the $t\bar{t}$ + jets, tW + jets, and VV + jets backgrounds lose roughly 44%, 47%, and 19% of events after we require $0.05 < \Delta R_{\ell\ell} < 2$ in cut 2, respectively.

Secondly, in Fig. 8(b), we present the $m_{\tau\tau}$ distributions after cut 2. As discussed above, $m_{\tau\tau}$ approximates the invariant mass of the tau pair in the $\tau^+\tau^-$ + jets, resulting in a peak at $m_{\tau\tau} \sim m_Z$. In addition, the tau pair from the $W^+W^- \rightarrow \tau^+\tau^-\nu_\tau\bar{\nu}_\tau$ process in the VV + jets background leads to a peak around $\sim 2m_W$. Therefore, the veto on $0 \leq m_{\tau\tau} \leq 200$ GeV in cut 3 significantly reduces the $\tau^+\tau^-$ + jets and VV + jets backgrounds. As shown in Table V, only $\sim 19\%$ and $\sim 58\%$ of events in the $\tau^+\tau^-$ + jets and VV + jets backgrounds remain after cut 3, respectively.

Thirdly, the distributions of the number of b -tagged jets after cut 3 are illustrated in Fig. 8(c). Since the jets induced by the b quarks from the $t\bar{t}$ + jets and tW + jets backgrounds have a high probability to be tagged as b -jets, most events from these two backgrounds have at least one b -tagged jet. As a result, the veto on b -tagged jets in cut 4 removes $\sim 63\%$ ($\sim 58\%$) of event in the $t\bar{t}$ + jets (tW + jets) background.

Finally, we demonstrate the $m_{\ell\ell}$ distributions in Fig. 8(d). As expected, the VV + jets background peaks around $m_{\ell\ell} \sim m_Z$, manifesting the Z pole. Furthermore, the $t\bar{t}$ + jets and tW + jets backgrounds tend to have larger $m_{\ell\ell}$ than the BMPs. Consequently, the

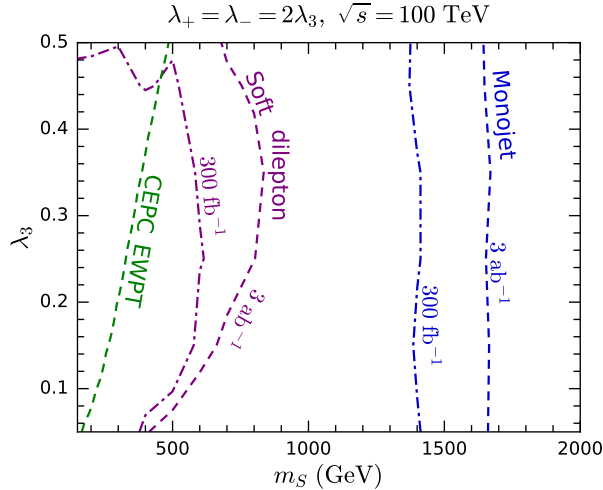


FIG. 9. Sensitivities of future pp and e^+e^- colliders presented in the m_S - λ_3 plane for $\lambda_+ = \lambda_- = 2\lambda_3$. The purple (blue) lines denote the expected 95% C.L. exclusion limits of the soft-dilepton + jets + \cancel{E}_T (monojet + \cancel{E}_T) channel at a 100 TeV pp collider with integrated luminosities 300 fb^{-1} and 3 ab^{-1} . The green line indicates the expected 95% C.L. exclusion limit of the future EWPT at the CEPC [63] (see Sec. V).

requirement of $m_{\ell\ell} \in [1, 3) \cup (3.2, 70] \text{ GeV}$ in cut 5 kills about 82%, 67%, and 63% of events in the $VV + \text{jets}$, $t\bar{t} + \text{jets}$, and $tW + \text{jets}$ backgrounds, respectively. On the other hand, since the SFOS lepton pair in the signal BMPs comes from the decay processes $\phi^0 \rightarrow a^0 \ell^+ \ell^-$, $S_2^\pm \rightarrow S_1^\pm \ell^+ \ell^-$, and $S_2^{2\pm} \rightarrow S_1^{2\pm} \ell^+ \ell^-$, its invariant mass $m_{\ell\ell}$ reflects the mass splittings of the dark sector scalars. As shown in Table II, BMP1, BMP2, BMP3, and BMP4 have descending $m_{\phi^0} - m_{a^0}$. Therefore, descending peaks exhibit accordingly in their $m_{\ell\ell}$ distributions.

Here we define six signal regions by requiring $m_{\ell\ell} \in [1, 10]$, $[1, 20]$, $[1, 40]$, $[1, 50]$, $[1, 60]$, and $[1, 70]$, dubbed SR-10, SR-20, SR-40, SR-50, SR-60, and SR-70, respectively. Table V also lists the visible cross sections and the signal significances of the four BMPs in the signal regions SR-60, SR-40, and SR-20. We find that BMP1 has the largest \mathcal{S} in SR-40, while the other three BMPs reach the largest \mathcal{S} in SR-20.

In Fig. 9, we show the expected 95% C.L. exclusion limit in the soft-dilepton + jets + \cancel{E}_T channel with the six signal regions combined at $\sqrt{s} = 100 \text{ TeV}$, presented in the m_S - λ_3 plane for $\lambda_+ = \lambda_- = 2\lambda_3$. With an integrated luminosity of 300 fb^{-1} (3 ab^{-1}), the 100 TeV soft-dilepton search could probe a region up to $m_S \sim 600$ (840) GeV. Although the soft-dilepton channel is more powerful than the monojet channel at the 13 TeV LHC, it becomes less sensitive at a 100 TeV machine.

V. INDIRECT PROBE WITH ELECTROWEAK OBLIQUE PARAMETERS

Since the sextuplet components participate electroweak gauge interactions, they could contribute to several electroweak precision observables at one-loop level [23]. Most of the

effects come from vacuum polarization diagrams of the electroweak gauge bosons and can be incorporated into the electroweak oblique parameters S , T , and U [93, 94], whose values can be determined in the EWPT. In this section, we explore the current EWPT constraint on the inert sextuplet model, as well as the future sensitivity.

S , T , and U are linear combinations of the $g^{\mu\nu}$ coefficients $\Pi_{PQ}(p^2)$ of the gauge boson vacuum polarizations contributed by new physics, defined as

$$S = \frac{4s_W^2 c_W^2}{\alpha} \left[\Pi'_{ZZ}(0) - \frac{c_W^2 - s_W^2}{s_W c_W} \Pi'_{ZA}(0) - \Pi'_{AA}(0) \right], \quad (36)$$

$$T = \frac{1}{\alpha} \left[\frac{\Pi_{WW}(0)}{m_W^2} - \frac{\Pi_{ZZ}(0)}{m_Z^2} \right], \quad (37)$$

$$U = \frac{4s_W^2}{\alpha} \left[\Pi'_{WW}(0) - c_W^2 \Pi'_{ZZ}(0) - 2s_W c_W \Pi'_{ZA}(0) - s_W^2 \Pi'_{AA}(0) \right], \quad (38)$$

where α is the fine structure constant, $s_W \equiv \sin \theta_W$, and $\Pi'_{PQ}(0) \equiv \partial \Pi_{PQ}(p^2) / \partial p^2|_{p^2=0}$. Note that the SM predicts $S = T = U = 0$. The one-loop contributions to $\Pi_{PQ}(p^2)$ by the dark sector bosons in the inert sextuplet model are given in Appendix B.

A $SU(2)_L$ multiplet with nonzero hypercharge split by the Higgs VEV typically gives nonzero S , T , and U [95, 96]. Nevertheless, if the interactions between the multiplet and the Higgs doublet respect a global $SU(2)_L \times SU(2)_R$ symmetry, a custodial $SU(2)_{L+R}$ symmetry [97] remains after electroweak symmetry breaking, resulting in vanishing T and U . In the inert sextuplet scalar model, the custodial symmetry corresponds to the condition

$$\lambda_- = \pm 2\lambda_3. \quad (39)$$

To make this clear, we construct two $SU(2)_R$ doublet \mathbf{H}^I and \mathbf{S}^I ($I = 1, 2$), whose components are $SU(2)_L$ doublets and sextuplets, respectively, given by

$$\mathbf{H}^{1,i} = \epsilon^{ij} H_j^\dagger, \quad \mathbf{H}^{2,i} = H^i, \quad (40)$$

$$\mathbf{S}^{1,ijklm} = \epsilon^{ip} \epsilon^{jq} \epsilon^{kr} \epsilon^{ls} \epsilon^{mt} S_{pqrst}^\dagger, \quad \mathbf{S}^{2,ijklm} = S^{ijklm}. \quad (41)$$

Thus, a generic potential respecting the global $SU(2)_L \times SU(2)_R$ symmetry can be written down as

$$\begin{aligned} V_{\text{cus}} &= \lambda_a \mathbf{H}_{I,i}^\dagger \mathbf{H}^{I,i} \mathbf{S}_{J,jklmn}^\dagger \mathbf{S}^{J,ijklm} + \lambda_b \mathbf{H}_{I,i}^\dagger \mathbf{S}_{J,pjklm}^\dagger \mathbf{S}^{J,ijklm} \mathbf{H}^{I,q} \epsilon^{ip} \epsilon_{nq} \\ &\quad + \lambda_c \mathbf{H}_{I,i}^\dagger \mathbf{S}^{I,ijklm} \mathbf{S}_{J,jklmn}^\dagger \mathbf{H}^{J,n} + \lambda_d \mathbf{H}_{I,i}^\dagger \mathbf{S}^{J,ijklm} \mathbf{S}_{K,jklmn}^\dagger \mathbf{H}^{L,n} \epsilon^{IK} \epsilon_{JL} \\ &= 4\lambda_a H_i^\dagger H^i S_{ijklmn}^\dagger S^{ijklm} + 2(\lambda_b + \lambda_c) H_i^\dagger S^{ijklm} S_{ijklmn}^\dagger H^j \\ &\quad + 2(\lambda_b + \lambda_d) H_i^\dagger S_{kmnpq}^\dagger S^{lmnpq} H^j \epsilon^{ik} \epsilon_{lj} \\ &\quad + (\lambda_c - \lambda_d) (H_i^\dagger H_j^\dagger S^{ijklm} S^{jpkrs} \epsilon_{kp} \epsilon_{lq} \epsilon_{mr} \epsilon_{ns} + \text{H.c.}). \end{aligned} \quad (42)$$

After electroweak symmetry breaking, such a potential would respect the custodial $SU(2)_{L+R}$

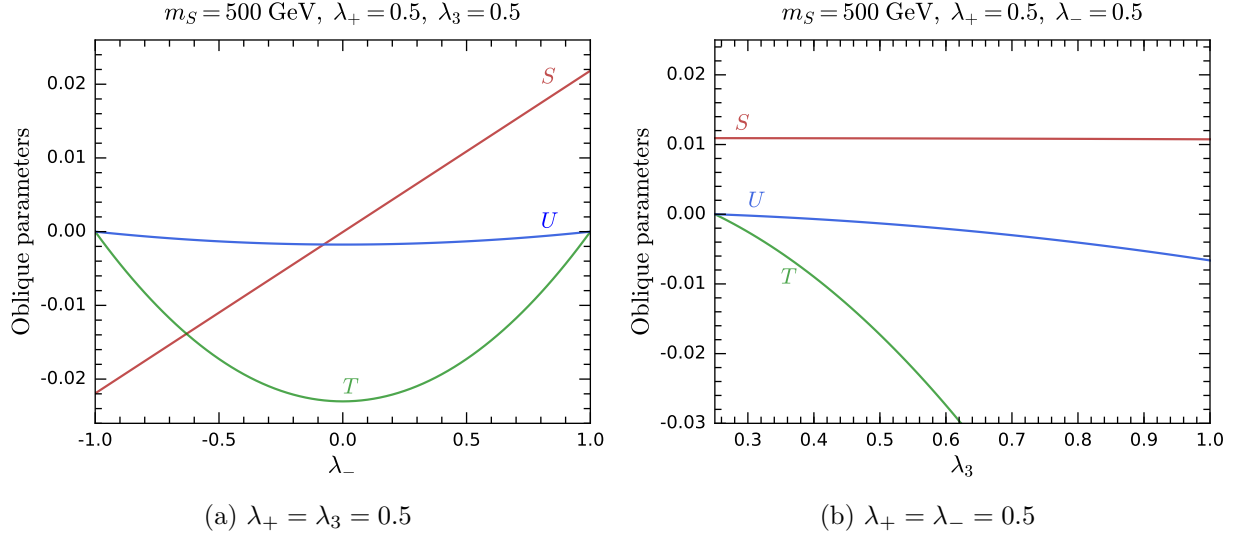


FIG. 10. Electroweak oblique parameters S , T , and U as functions of λ_- for $\lambda_+ = \lambda_3 = 0.5$ (a) and of λ_3 for $\lambda_+ = \lambda_- = 0.5$ (b). For both panels, $m_S = 500 \text{ GeV}$.

symmetry. As discussed above, the $4\lambda_a H_i^\dagger H^i S_{jklmn}^\dagger S^{jklmn}$ term is not independent. Compared with the potential (6), we find that

$$\lambda_1 = 2(\lambda_b + \lambda_c), \quad \lambda_2 = 2(\lambda_b + \lambda_d), \quad \lambda_3 = \lambda_c - \lambda_d, \quad (43)$$

which lead to $\lambda_- = \lambda_1 - \lambda_2 = 2\lambda_3$. Therefore, $\lambda_- = 2\lambda_3$ is a condition for respecting the custodial symmetry. On the other hand, if we define

$$\mathbf{S}^{1,ijklm} = -\epsilon^{ip} \epsilon^{jq} \epsilon^{kr} \epsilon^{ls} \epsilon^{mt} S_{pqrst}^\dagger, \quad \mathbf{S}^{2,ijklm} = S^{ijklm}, \quad (44)$$

instead of Eq. (41), we would prove that $\lambda_- = -2\lambda_3$ is another condition for the custodial symmetry.

In Fig. 10(a), we plot the electroweak oblique parameters S , T , and U as functions of λ_- for $m_S = 500 \text{ GeV}$ and $\lambda_+ = \lambda_3 = 0.5$. In this case, S increases as λ_- increases, and T and U are not positive. At $\lambda_- = 0$, S vanishes, while T and U reach their minimums. For $\lambda_- = \pm 1$, the custodial symmetry condition $\lambda_- = \pm 2\lambda_3$ is satisfied, leading to $T = U = 0$. In Fig. 10(b), the oblique parameters are presented as functions of λ_3 for $m_S = 500 \text{ GeV}$ and $\lambda_+ = \lambda_- = 0.5$. In this case, S hardly shows dependence on λ_3 , while T and U decrease as λ_3 increases. In both cases, U is always quite small, and this is typical in electroweak multiplet DM models [36, 38]. Therefore, we neglect U in the following analysis.

Assuming $U = 0$, the Gfitter Group performs a global fit of current EWPT data and gives [92]

$$S = 0.06 \pm 0.09, \quad T = 0.10 \pm 0.07, \quad \rho_{ST} = 0.91, \quad (45)$$

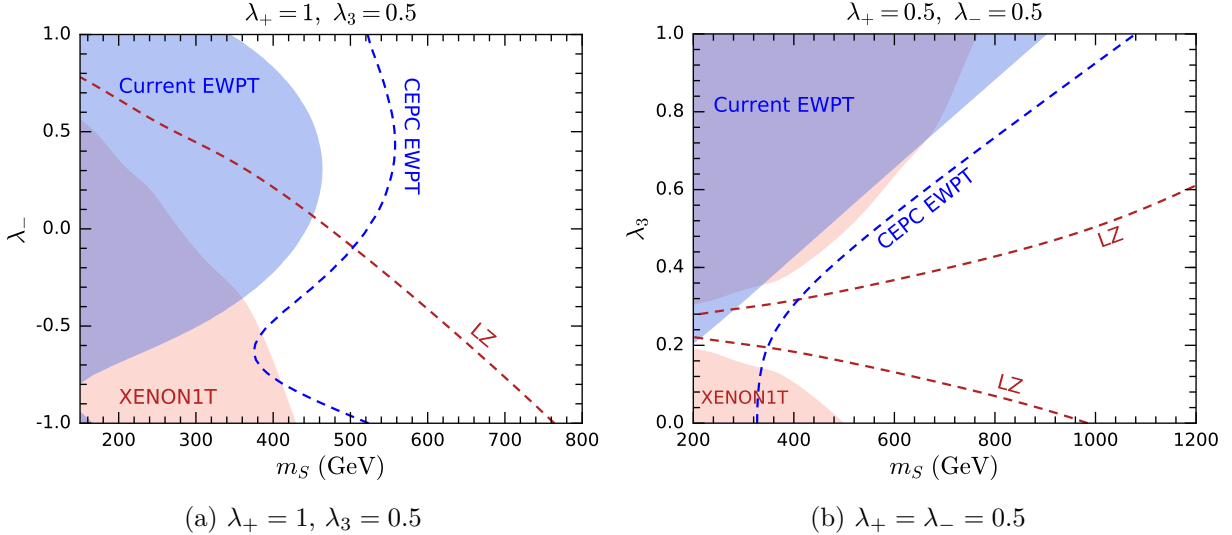


FIG. 11. Current constraints and future sensitivities of EWPT and direct detection in the m_S - λ plane for $\lambda_+ = 1$ and $\lambda_3 = 0.5$ (a) and in the m_S - λ_3 plane for $\lambda_+ = \lambda_- = 0.5$ (b). The blue shade regions are excluded at 95% C.L. by the global fit of current EWPT data from the Gfitter Group [92]. The blue dashed lines denote the expected 95% C.L. exclusion limits of the future EWPT at the CEPC [63]. The red shade regions are excluded at 90% C.L. by the XENON1T direct detection experiment [98]. The red dashed lines indicate the expected 90% C.L. exclusion limits of the future LZ direct detection experiment [99].

where ρ_{ST} is the correlation coefficient between S and T . We use this result to constrain the inert sextuplet model, as shown in Fig. 11. We find that the current EWPT excludes a region with $m_S \lesssim 460$ GeV in Fig. 11(a) for $\lambda_+ = 1$ and $\lambda_3 = 0.5$, and also excludes a region up to $m_S \sim 900$ GeV in Fig. 11(b) for $\lambda_+ = \lambda_- = 0.5$. Moreover, in Fig. 7 for the relation $\lambda_+ = \lambda_- = 2\lambda_3$, a region with $m_S \lesssim 140$ GeV and $\lambda_3 \leq 0.5$ is excluded by the current EWPT. Such a constraint is more stringent than the constraint from the 13 TeV monojet search, but looser than that from the 13 TeV soft-dilepton search.

Future e^+e^- collider projects could greatly improve the measurement of the electroweak oblique parameters, providing a powerful indirect probe to the sextuplet scalar. For instance, the CEPC EWPT could reach a precision of [63]

$$\sigma_S = 0.01, \quad \sigma_T = 0.01, \quad \rho_{ST} = 0.62, \quad (46)$$

where σ_S and σ_T are the 1σ uncertainties of S and T , respectively. Figure 11 shows the expected 95% C.L. exclusion limits of the CEPC EWPT. We find that CEPC could reach up to $m_S \sim 560$ GeV in Fig. 11(a) and $m_S \sim 1.08$ TeV in Fig. 11(b). In Fig. 9 for the relation $\lambda_+ = \lambda_- = 2\lambda_3$, the CEPC EWPT could probe a region with $m_S \lesssim 500$ GeV and $\lambda_3 \leq 0.5$.

For comparison, in Fig. 11 we also demonstrate the regions excluded at 90% C.L. by the

XENON1T direct detection experiment [98], as well as the expected 90% C.L. exclusion limits of the future LZ direct detection experiment [99]. Note that the condition (26) corresponds to $\lambda_- = 1$ for $\lambda_+ = 1$ and $\lambda_3 = 0.5$ in Fig. 11(a) and to $\lambda_3 = 0.25$ for $\lambda_+ = \lambda_- = 0.5$ in Fig. 11(b). Therefore, direct detection loses sensitivity in the regions around $\lambda_- \sim 1$ and $\lambda_3 \sim 0.25$, respectively. Nevertheless, the CEPC EWPT provides a complementary approach to such regions.

VI. CONCLUSIONS

In this work, we have investigated a SM extension with an inert $SU(2)_L$ sextuplet scalar of hypercharge 1/2. After electroweak symmetry breaking, the quartic couplings between the sextuplet and the Higgs doublet split the sextuplet components. Thus, the mass eigenstates in the dark sector include one triply charged scalar $S^{3\pm}$, two doubly charged scalars $S_{1,2}^{2\pm}$, two singly charged scalars $S_{1,2}^{\pm}$, and two neutral real scalars ϕ^0 and a^0 . When the quartic couplings satisfy $\lambda_3 \geq 0$ and $|\lambda_-| \leq 2\lambda_3$, a^0 is the lightest dark sector scalar, acting as a viable DM candidate.

The mass spectrum in this model is typically compressed, leading to 3-body decays of the dark sector scalars mediated by the W , Z , and Higgs bosons. After pairs of these scalars are produced by electroweak processes at the LHC or a future 100 TeV pp collider, the resulting decay products are typically soft. This motivates us to consider the monojet + \cancel{E}_T and soft-dilepton + jets + \cancel{E}_T final states to search for the dark sector scalars at pp colliders. When the quartic couplings satisfy a particular relation (26), the DM-nucleon scattering is absent at tree level and DM direct detection experiments hardly probe the inert sextuplet model. In this case, collider searches provide complementary approaches to this model.

Based on Monte Carlo simulation, we have derived the constraints from current LHC searches and have further evaluated the sensitivities at a 100 TeV pp collider. We have found that the 13 TeV monojet search excludes the parameter space up to $m_S \sim 85$ GeV, while the 13 TeV soft-dilepton search is more powerful, excluding the parameter space up to $m_S \sim 210$ GeV. At a 100 TeV pp collider, nonetheless, the monojet channel is much more sensitive than the soft-dilepton channel for probing the high mass region. This is because the mass spectrum becomes more compressed at higher mass scales, leading to softer decay products. With an integrated luminosity of 3 ab^{-1} at $\sqrt{s} = 100$ TeV, the monojet (soft-dilepton) search could explore the parameter space up to $m_S \sim 1.65$ (0.84) TeV.

Since the sextuplet components contribute to the electroweak oblique parameters at one-loop level, EWPT provides an indirectly path to probe the model. We have found that the current EWPT excludes a parameter region with $m_S \lesssim 900$ GeV for $\lambda_+ = \lambda_- = 0.5$, while the future CEPC EWPT could probe the parameter space up to $m_S \sim 1.08$ TeV.

ACKNOWLEDGMENTS

This work is supported in part by the National Natural Science Foundation of China under Grants No. 11805288, No. 11875327, and No. 11905300, the China Postdoctoral Science Foundation under Grant No. 2018M643282, the Natural Science Foundation of Guangdong Province under Grant No. 2016A030313313, the Fundamental Research Funds for the Central Universities, and the Sun Yat-Sen University Science Foundation.

Appendix A: Electroweak gauge couplings of the sextuplet scalar

From Eqs. (4) and (5), we derive the electroweak gauge couplings of the sextuplet scalar S . The Lagrangian for the trilinear gauge couplings reads

$$\begin{aligned}
\mathcal{L}_{\text{gauge}}^{\text{tri}} = & eA_\mu \left[3(S^{3+})^\dagger i \overleftrightarrow{\partial}^\mu S^{3+} + 2(S^{2+})^\dagger i \overleftrightarrow{\partial}^\mu S^{2+} + (S^+)^\dagger i \overleftrightarrow{\partial}^\mu S^+ \right. \\
& \left. - (S^-)^\dagger i \overleftrightarrow{\partial}^\mu S^- - 2(S^{2-})^\dagger i \overleftrightarrow{\partial}^\mu S^{2-} \right] \\
& + \frac{gZ_\mu}{2c_W} \left[(6c_W^2 - 1)(S^{3+})^\dagger i \overleftrightarrow{\partial}^\mu S^{3+} + (4c_W^2 - 1)(S^{2+})^\dagger i \overleftrightarrow{\partial}^\mu S^{2+} + (2c_W^2 - 1)(S^+)^\dagger i \overleftrightarrow{\partial}^\mu S^+ \right. \\
& \left. - (S^0)^\dagger i \overleftrightarrow{\partial}^\mu S^0 - (2c_W^2 + 1)(S^-)^\dagger i \overleftrightarrow{\partial}^\mu S^- - (4c_W^2 + 1)(S^{2-})^\dagger i \overleftrightarrow{\partial}^\mu S^{2-} \right] \\
& + g \left\{ \frac{\sqrt{10}}{2} W_\mu^+ \left[(S^{3+})^\dagger i \overleftrightarrow{\partial}^\mu S^{2+} + (S^-)^\dagger i \overleftrightarrow{\partial}^\mu S^{2-} \right] + 2W_\mu^+ \left[(S^{2+})^\dagger i \overleftrightarrow{\partial}^\mu S^+ + (S^0)^\dagger i \overleftrightarrow{\partial}^\mu S^- \right] \right. \\
& \left. + \frac{3\sqrt{2}}{2} W_\mu^+ (S^+)^\dagger i \overleftrightarrow{\partial}^\mu S^0 + \text{H.c.} \right\}, \tag{A1}
\end{aligned}$$

where $\phi_1 \overleftrightarrow{\partial}^\mu \phi_2 \equiv \phi_1 \partial^\mu \phi_2 - (\partial^\mu \phi_1) \phi_2$.

The quartic gauge couplings are given by

$$\begin{aligned}
\mathcal{L}_{\text{gauge}}^{\text{qua}} = & e^2 A_\mu A^\mu \left(9|S^{3+}|^2 + 4|S^{2+}|^2 + |S^+|^2 + |S^-|^2 + 4|S^{2-}|^2 \right) \\
& + \frac{g^2}{4c_W^2} Z_\mu Z^\mu \left[(6c_W^2 - 1)^2 |S^{3+}|^2 + (4c_W^2 - 1)^2 |S^{2+}|^2 + (2c_W^2 - 1)^2 |S^+|^2 \right. \\
& \left. + |S^0|^2 + (2c_W^2 + 1)^2 |S^-|^2 + (4c_W^2 + 1)^2 |S^{2-}|^2 \right] \\
& + \frac{eg}{c_W} A_\mu Z^\mu \left[3(6c_W^2 - 1) |S^{3+}|^2 + 2(4c_W^2 - 1) |S^{2+}|^2 + (2c_W^2 - 1) |S^+|^2 \right. \\
& \left. + (2c_W^2 + 1) |S^-|^2 + 2(4c_W^2 + 1) |S^{2-}|^2 \right] \\
& + g^2 W_\mu^+ W^{-\mu} \left[\frac{5}{2} (|S^{3+}|^2 + |S^{2-}|^2) + \frac{13}{2} (|S^{2+}|^2 + |S^-|^2) + \frac{17}{2} (|S^+|^2 + |S^0|^2) \right] \\
& + g^2 \left(W_\mu^+ W^{+\mu} \left\{ \sqrt{10} [(S^{3+})^\dagger S^+ + (S^0)^\dagger S^{2-}] + 3\sqrt{2} [(S^{2+})^\dagger S^0 + (S^+)^\dagger S^-] \right\} + \text{H.c.} \right) \\
& + g \left(W_\mu^+ \left\{ \frac{\sqrt{10}}{2} \left[5eA^\mu + \frac{g}{c_W} (5c_W^2 - 1) Z_\mu \right] (S^{3+})^\dagger S^{2+} \right. \right.
\end{aligned}$$

$$\begin{aligned}
& + 2 \left[3eA_\mu + \frac{g}{c_W}(3c_W^2 - 1)Z_\mu \right] (S^{2+})^\dagger S^+ \\
& + \frac{3\sqrt{2}}{2} \left[eA_\mu + \frac{g}{c_W}(c_W^2 - 1)Z_\mu \right] (S^+)^\dagger S^0 \\
& - 2 \left[eA_\mu + \frac{g}{c_W}(c_W^2 + 1)Z_\mu \right] (S^0)^\dagger S^- \\
& - \frac{\sqrt{10}}{2} \left[3eA_\mu + \frac{g}{c_W}(3c_W^2 + 1)Z_\mu \right] (S^-)^\dagger S^{2-} \left. \right\} + \text{H.c.} \Big). \tag{A2}
\end{aligned}$$

Appendix B: Vacuum polarizations of electroweak gauge bosons

In this appendix, we explicitly list the one-loop contributions to gauge boson vacuum polarizations $\Pi_{PQ}(p^2)$ by the dark sector scalar bosons in the inert sextuplet model. We express the results with the Passiano–Veltman scalar functions A_0 and B_{00} [100], whose definitions are consistent with Ref. [101]. In our calculation, the numerical values of these functions are provided by `LoopTools` [102].

The photon vacuum polarization contributed by the dark sector scalars is

$$\begin{aligned}
\Pi_{AA}(p^2) = \frac{e^2}{16\pi^2} \{ & 18[2B_{00}(p^2, m_{S^{3\pm}}^2, m_{S^{3\pm}}^2) - A_0(m_{S^{3\pm}}^2)] \\
& + 8[2B_{00}(p^2, m_{S_1^{2\pm}}^2, m_{S_1^{2\pm}}^2) - A_0(m_{S_1^{2\pm}}^2) + 2B_{00}(p^2, m_{S_2^{2\pm}}^2, m_{S_2^{2\pm}}^2) - A_0(m_{S_2^{2\pm}}^2)] \\
& + 2[2B_{00}(p^2, m_{S_1^\pm}^2, m_{S_1^\pm}^2) - A_0(m_{S_1^\pm}^2) + 2B_{00}(p^2, m_{S_2^\pm}^2, m_{S_2^\pm}^2) - A_0(m_{S_2^\pm}^2)] \}. \tag{B1}
\end{aligned}$$

The photon- Z vacuum polarization reads

$$\begin{aligned}
\Pi_{AZ}(p^2) = \frac{e^2}{16\pi^2 s_W c_W} \{ & 3(5 - 6s_W^2)[2B_{00}(p^2, m_{S^{3\pm}}^2, m_{S^{3\pm}}^2) - A_0(m_{S^{3\pm}}^2)] \\
& + 2(3 + 2s_{2+}^2 - 4s_W^2)[2B_{00}(p^2, m_{S_1^{2\pm}}^2, m_{S_1^{2\pm}}^2) - A_0(m_{S_1^{2\pm}}^2)] \\
& + 2(5 - 2s_{2+}^2 - 4s_W^2)[2B_{00}(p^2, m_{S_2^{2\pm}}^2, m_{S_2^{2\pm}}^2) - A_0(m_{S_2^{2\pm}}^2)] \\
& + (1 + 2s_+^2 - 2s_W^2)[2B_{00}(p^2, m_{S_1^\pm}^2, m_{S_1^\pm}^2) - A_0(m_{S_1^\pm}^2)] \\
& + (3 - 2s_+^2 - 2s_W^2)[2B_{00}(p^2, m_{S_2^\pm}^2, m_{S_2^\pm}^2) - A_0(m_{S_2^\pm}^2)] \}, \tag{B2}
\end{aligned}$$

where $s_{2+} \equiv \sin \theta_{2+}$ and $s_+ \equiv \sin \theta_+$. The Z boson vacuum polarization is given by

$$\begin{aligned}
\Pi_{ZZ}(p^2) = \frac{e^2}{32\pi^2 s_W^2 c_W^2} \{ & 2(5 - 6s_W^2)^2 B_{00}(p^2, m_{S^{3\pm}}^2, m_{S^{3\pm}}^2) + 2B_{00}(p^2, m_{\phi^0}^2, m_{a^0}^2) \\
& + 2(3 + 2s_{2+}^2 - 4s_W^2)^2 B_{00}(p^2, m_{S_1^{2\pm}}^2, m_{S_1^{2\pm}}^2) + 16s_{2+}^2 c_{2+}^2 B_{00}(p^2, m_{S_1^{2\pm}}^2, m_{S_2^{2\pm}}^2) \\
& + 2(5 - 2s_{2+}^2 - 4s_W^2)^2 B_{00}(p^2, m_{S_2^{2\pm}}^2, m_{S_2^{2\pm}}^2) \\
& + 2(1 + 2s_+^2 - 2s_W^2)^2 B_{00}(p^2, m_{S_1^\pm}^2, m_{S_1^\pm}^2) + 16s_+^2 c_+^2 B_{00}(p^2, m_{S_2^\pm}^2, m_{S_1^\pm}^2) \\
& + 2(3 - 2s_+^2 - 2s_W^2)^2 B_{00}(p^2, m_{S_2^\pm}^2, m_{S_2^\pm}^2) \}
\end{aligned}$$

$$\begin{aligned}
& - (5 - 6s_W^2)^2 A_0(m_{S_{3\pm}}^2) - A_0(m_{\phi^0}^2)/2 - A_0(m_{a^0}^2)/2 \\
& - [(3 - 4s_W^2)^2 c_{2+}^2 + (5 - 4s_W^2)^2 s_{2+}^2] A_0(m_{S_1^{2\pm}}^2) \\
& - [(3 - 4s_W^2)^2 s_{2+}^2 + (5 - 4s_W^2)^2 c_{2+}^2] A_0(m_{S_2^{2\pm}}^2) \\
& - [(1 - 2s_W^2)^2 c_+^2 + (3 - 2s_W^2)^2 s_+^2] A_0(m_{S_1^\pm}^2) \\
& - [(1 - 2s_W^2)^2 s_+^2 + (3 - 2s_W^2)^2 c_+^2] A_0(m_{S_2^\pm}^2), \tag{B3}
\end{aligned}$$

where $c_{2+} \equiv \cos \theta_{2+}$ and $c_+ \equiv \cos \theta_+$. The W boson vacuum polarization is

$$\begin{aligned}
\Pi_{WW}(p^2) = & \frac{e^2}{16\pi^2 s_W^2} [10c_{2+}^2 B_{00}(p^2, m_{S_{3\pm}}^2, m_{S_1^{2\pm}}^2) + 10s_{2+}^2 B_{00}(p^2, m_{S_{3\pm}}^2, m_{S_2^{2\pm}}^2) \\
& + 4(2c_+ c_{2+} - \sqrt{5/2} s_+ s_{2+})^2 B_{00}(p^2, m_{S_1^{2\pm}}^2, m_{S_1^\pm}^2) \\
& + 4(2s_+ c_{2+} + \sqrt{5/2} c_+ s_{2+})^2 B_{00}(p^2, m_{S_1^{2\pm}}^2, m_{S_2^\pm}^2) \\
& + 4(2c_+ s_{2+} + \sqrt{5/2} s_+ c_{2+})^2 B_{00}(p^2, m_{S_2^{2\pm}}^2, m_{S_1^\pm}^2) \\
& + 4(2s_+ s_{2+} - \sqrt{5/2} c_+ c_{2+})^2 B_{00}(p^2, m_{S_2^{2\pm}}^2, m_{S_2^\pm}^2) \\
& + 4(3c_+/2 - \sqrt{2} s_+)^2 B_{00}(p^2, m_{S_1^\pm}^2, m_{\phi^0}^2) \\
& + 4(3c_+/2 + \sqrt{2} s_+)^2 B_{00}(p^2, m_{S_1^\pm}^2, m_{a^0}^2) \\
& + 4(3s_+/2 + \sqrt{2} c_+)^2 B_{00}(p^2, m_{S_2^\pm}^2, m_{\phi^0}^2) \\
& + 4(3s_+/2 - \sqrt{2} c_+)^2 B_{00}(p^2, m_{S_2^\pm}^2, m_{a^0}^2) \\
& - 5A(m_{S_{3\pm}}^2)/2 - (13/2 - 4s_{2+}^2)A_0(m_{S_1^{2\pm}}^2) - (5/2 + 4s_{2+}^2)A_0(m_{S_2^{2\pm}}^2) \\
& - (17/2 - 2s_+^2)A_0(m_{S_1^\pm}^2) - (13/2 + 2s_+^2)A_0(m_{S_2^\pm}^2) \\
& - 17A_0(m_{\phi^0}^2)/4 - 17A_0(m_{a^0}^2)/4]. \tag{B4}
\end{aligned}$$

-
- [1] S. L. Glashow, “Partial Symmetries of Weak Interactions,” *Nucl. Phys.* **22** (1961) 579–588.
- [2] S. Weinberg, “A Model of Leptons,” *Phys. Rev. Lett.* **19** (1967) 1264–1266.
- [3] A. Salam, “Weak and Electromagnetic Interactions,” *Conf. Proc.* **C680519** (1968) 367–377.
- [4] G. Bertone, D. Hooper, and J. Silk, “Particle dark matter: Evidence, candidates and constraints,” *Phys. Rept.* **405** (2005) 279–390, [arXiv:hep-ph/0404175 \[hep-ph\]](#).
- [5] J. L. Feng, “Dark Matter Candidates from Particle Physics and Methods of Detection,” *Ann. Rev. Astron. Astrophys.* **48** (2010) 495–545, [arXiv:1003.0904 \[astro-ph.CO\]](#).
- [6] B.-L. Young, “A survey of dark matter and related topics in cosmology,” *Front. Phys.(Beijing)* **12** (2017) 121201. [Erratum: *Front. Phys.(Beijing)*12,no.2,121202(2017)].
- [7] R. Mahbubani and L. Senatore, “The Minimal model for dark matter and unification,” *Phys. Rev.* **D73** (2006) 043510, [arXiv:hep-ph/0510064 \[hep-ph\]](#).

- [8] M. Cirelli, N. Fornengo, and A. Strumia, “Minimal dark matter,” *Nucl. Phys.* **B753** (2006) 178–194, [arXiv:hep-ph/0512090](#) [hep-ph].
- [9] R. Barbieri, L. J. Hall, and V. S. Rychkov, “Improved naturalness with a heavy Higgs: An Alternative road to LHC physics,” *Phys. Rev.* **D74** (2006) 015007, [arXiv:hep-ph/0603188](#) [hep-ph].
- [10] M. Gustafsson, E. Lundstrom, L. Bergstrom, and J. Edsjo, “Significant Gamma Lines from Inert Higgs Dark Matter,” *Phys. Rev. Lett.* **99** (2007) 041301, [arXiv:astro-ph/0703512](#) [ASTRO-PH].
- [11] M. Cirelli, A. Strumia, and M. Tamburini, “Cosmology and Astrophysics of Minimal Dark Matter,” *Nucl. Phys.* **B787** (2007) 152–175, [arXiv:0706.4071](#) [hep-ph].
- [12] Q.-H. Cao, E. Ma, and G. Rajasekaran, “Observing the Dark Scalar Doublet and its Impact on the Standard-Model Higgs Boson at Colliders,” *Phys. Rev.* **D76** (2007) 095011, [arXiv:0708.2939](#) [hep-ph].
- [13] P. Fileviez Perez, H. H. Patel, M. Ramsey-Musolf, and K. Wang, “Triplet Scalars and Dark Matter at the LHC,” *Phys. Rev.* **D79** (2009) 055024, [arXiv:0811.3957](#) [hep-ph].
- [14] M. Cirelli and A. Strumia, “Minimal Dark Matter: Model and results,” *New J. Phys.* **11** (2009) 105005, [arXiv:0903.3381](#) [hep-ph].
- [15] T. Hambye, F. S. Ling, L. Lopez Honorez, and J. Rocher, “Scalar Multiplet Dark Matter,” *JHEP* **07** (2009) 090, [arXiv:0903.4010](#) [hep-ph]. [Erratum: JHEP05,066(2010)].
- [16] T. Araki, C. Q. Geng, and K. I. Nagao, “Dark Matter in Inert Triplet Models,” *Phys. Rev.* **D83** (2011) 075014, [arXiv:1102.4906](#) [hep-ph].
- [17] T. Cohen, J. Kearney, A. Pierce, and D. Tucker-Smith, “Singlet-Doublet Dark Matter,” *Phys. Rev.* **D85** (2012) 075003, [arXiv:1109.2604](#) [hep-ph].
- [18] Y. Cai, W. Chao, and S. Yang, “Scalar Septuplet Dark Matter and Enhanced $h \rightarrow \gamma\gamma$ Decay Rate,” *JHEP* **12** (2012) 043, [arXiv:1208.3949](#) [hep-ph].
- [19] F.-X. Josse-Michaux and E. Molinaro, “Triplet scalar dark matter and leptogenesis in an inverse seesaw model of neutrino mass generation,” *Phys. Rev.* **D87** (2013) 036007, [arXiv:1210.7202](#) [hep-ph].
- [20] K. Earl, K. Hartling, H. E. Logan, and T. Pilkington, “Constraining models with a large scalar multiplet,” *Phys. Rev.* **D88** (2013) 015002, [arXiv:1303.1244](#) [hep-ph].
- [21] S. S. AbdusSalam and T. A. Chowdhury, “Scalar Representations in the Light of Electroweak Phase Transition and Cold Dark Matter Phenomenology,” *JCAP* **1405** (2014) 026, [arXiv:1310.8152](#) [hep-ph].
- [22] O. Fischer and J. J. van der Bij, “The scalar Singlet-Triplet Dark Matter Model,” *JCAP* **1401** (2014) 032, [arXiv:1311.1077](#) [hep-ph].
- [23] K. Earl, K. Hartling, H. E. Logan, and T. Pilkington, “Two viable large scalar multiplet models with a Z_2 symmetry,” *Phys. Rev.* **D90** (2014) 055029, [arXiv:1311.3656](#) [hep-ph]. [Erratum: Phys. Rev.D92,no.3,039902(2015)].

- [24] A. Dedes and D. Karamitros, “Doublet-Triplet Fermionic Dark Matter,” *Phys. Rev.* **D89** (2014) 115002, [arXiv:1403.7744 \[hep-ph\]](#).
- [25] S. Yaser Ayazi and S. M. Firouzabadi, “Constraining Inert Triplet Dark Matter by the LHC and FermiLAT,” *JCAP* **1411** (2014) 005, [arXiv:1408.0654 \[hep-ph\]](#).
- [26] K. Harigaya, K. Ichikawa, A. Kundu, S. Matsumoto, and S. Shirai, “Indirect Probe of Electroweak-Interacting Particles at Future Lepton Colliders,” *JHEP* **09** (2015) 105, [arXiv:1504.03402 \[hep-ph\]](#).
- [27] B. Ostdiek, “Constraining the minimal dark matter fiveplet with LHC searches,” *Phys. Rev.* **D92** (2015) 055008, [arXiv:1506.03445 \[hep-ph\]](#).
- [28] M. Cirelli, T. Hambye, P. Panci, F. Sala, and M. Taoso, “Gamma ray tests of Minimal Dark Matter,” *JCAP* **1510** (2015) 026, [arXiv:1507.05519 \[hep-ph\]](#).
- [29] C. Garcia-Cely, A. Ibarra, A. S. Lamperstorfer, and M. H. G. Tytgat, “Gamma-rays from Heavy Minimal Dark Matter,” *JCAP* **1510** (2015) 058, [arXiv:1507.05536 \[hep-ph\]](#).
- [30] C. Cai, Z.-M. Huang, Z. Kang, Z.-H. Yu, and H.-H. Zhang, “Perturbativity Limits for Scalar Minimal Dark Matter with Yukawa Interactions: Septuplet,” *Phys. Rev.* **D92** (2015) 115004, [arXiv:1510.01559 \[hep-ph\]](#).
- [31] T. M. P. Tait and Z.-H. Yu, “Triplet-Quadruplet Dark Matter,” *JHEP* **03** (2016) 204, [arXiv:1601.01354 \[hep-ph\]](#).
- [32] S. Banerjee, S. Matsumoto, K. Mukaida, and Y.-L. S. Tsai, “WIMP Dark Matter in a Well-Tempered Regime: A case study on Singlet-Doublets Fermionic WIMP,” *JHEP* **11** (2016) 070, [arXiv:1603.07387 \[hep-ph\]](#).
- [33] N. Khan, “Exploring the hyperchargeless Higgs triplet model up to the Planck scale,” *Eur. Phys. J.* **C78** (2018) 341, [arXiv:1610.03178 \[hep-ph\]](#).
- [34] H. E. Logan and T. Pilkington, “Large scalar multiplet dark matter in the high-mass region,” *Phys. Rev.* **D96** (2017) 015030, [arXiv:1610.08835 \[hep-ph\]](#).
- [35] W.-B. Lu and P.-H. Gu, “Mixed Inert Scalar Triplet Dark Matter, Radiative Neutrino Masses and Leptogenesis,” *Nucl. Phys.* **B924** (2017) 279–311, [arXiv:1611.02106 \[hep-ph\]](#).
- [36] C. Cai, Z.-H. Yu, and H.-H. Zhang, “CEPC Precision of Electroweak Oblique Parameters and Weakly Interacting Dark Matter: the Fermionic Case,” *Nucl. Phys.* **B921** (2017) 181–210, [arXiv:1611.02186 \[hep-ph\]](#).
- [37] T. A. Chowdhury and S. Nasri, “The Sommerfeld Enhancement in the Scotogenic Model with Large Electroweak Scalar Multiplets,” *JCAP* **1701** (2017) 041, [arXiv:1611.06590 \[hep-ph\]](#).
- [38] C. Cai, Z.-H. Yu, and H.-H. Zhang, “CEPC Precision of Electroweak Oblique Parameters and Weakly Interacting Dark Matter: the Scalar Case,” *Nucl. Phys.* **B924** (2017) 128–152, [arXiv:1705.07921 \[hep-ph\]](#).
- [39] X. Liu and L. Bian, “Dark matter and electroweak phase transition in the mixed scalar

- dark matter model,” *Phys. Rev.* **D97** (2018) 055028, [arXiv:1706.06042 \[hep-ph\]](#).
- [40] Q.-F. Xiang, X.-J. Bi, P.-F. Yin, and Z.-H. Yu, “Exploring Fermionic Dark Matter via Higgs Boson Precision Measurements at the Circular Electron Positron Collider,” *Phys. Rev.* **D97** (2018) 055004, [arXiv:1707.03094 \[hep-ph\]](#).
- [41] J.-W. Wang, X.-J. Bi, Q.-F. Xiang, P.-F. Yin, and Z.-H. Yu, “Exploring triplet-quadruplet fermionic dark matter at the LHC and future colliders,” *Phys. Rev. D* **97** (2018) 035021, [arXiv:1711.05622 \[hep-ph\]](#).
- [42] C. Cai, Z. Kang, Z. Luo, Z.-H. Yu, and H.-H. Zhang, “Scalar quintuplet minimal dark matter with Yukawa interactions: perturbative up to the Planck scale,” *Chin. Phys.* **C43** (2019) 023102, [arXiv:1711.07396 \[hep-ph\]](#).
- [43] L. Lopez Honorez, M. H. G. Tytgat, P. Tziveloglou, and B. Zaldivar, “On Minimal Dark Matter coupled to the Higgs,” *JHEP* **04** (2018) 011, [arXiv:1711.08619 \[hep-ph\]](#).
- [44] C. Cai, Z. Kang, H.-H. Zhang, and Y.-P. Zeng, “Minimal dark matter in $SU(2)_L \times U(1)_Y \times U(1)_{B-L}$,” *Phys. Lett.* **B784** (2018) 385–391, [arXiv:1801.05594 \[hep-ph\]](#).
- [45] A. Dutta Banik, A. K. Saha, and A. Sil, “Scalar assisted singlet doublet fermion dark matter model and electroweak vacuum stability,” *Phys. Rev.* **D98** (2018) 075013, [arXiv:1806.08080 \[hep-ph\]](#).
- [46] P.-H. Gu and H.-J. He, “TeV Scale Neutrino Mass Generation, Minimal Inelastic Dark Matter, and High Scale Leptogenesis,” *Phys. Rev.* **D99** (2019) 015025, [arXiv:1808.09377 \[hep-ph\]](#).
- [47] A. Betancur and Ó. Zapata, “Phenomenology of doublet-triplet fermionic dark matter in nonstandard cosmology and multicomponent dark sectors,” *Phys. Rev.* **D98** (2018) 095003, [arXiv:1809.04990 \[hep-ph\]](#).
- [48] K. Kadota and A. Spray, “Electroweak Multiplet Dark Matter at Future Lepton Colliders,” *JHEP* **02** (2019) 017, [arXiv:1811.00560 \[hep-ph\]](#).
- [49] J.-W. Wang, X.-J. Bi, P.-F. Yin, and Z.-H. Yu, “Impact of Fermionic Electroweak Multiplet Dark Matter on Vacuum Stability with One-loop Matching,” *Phys. Rev.* **D99** (2019) 055009, [arXiv:1811.08743 \[hep-ph\]](#).
- [50] A. Filimonova and S. Westhoff, “Long live the Higgs portal!,” *JHEP* **02** (2019) 140, [arXiv:1812.04628 \[hep-ph\]](#).
- [51] W. Chao, G.-J. Ding, X.-G. He, and M. Ramsey-Musolf, “Scalar Electroweak Multiplet Dark Matter,” *JHEP* **08** (2019) 058, [arXiv:1812.07829 \[hep-ph\]](#).
- [52] T. Abe and R. Sato, “Current status and future prospects of the singlet-doublet dark matter model with CP-violation,” *Phys. Rev.* **D99** (2019) 035012, [arXiv:1901.02278 \[hep-ph\]](#).
- [53] C. Cai and H.-H. Zhang, “Minimal asymptotically safe dark matter,” *Phys. Lett.* **B798** (2019) 134947, [arXiv:1905.04227 \[hep-ph\]](#).

- [54] Y. Cheng and W. Liao, “Fate of the false vacuum in a singlet-doublet fermion extension model with RG-improved effective action,” *Phys. Rev. D* **101** (2020) 055038, [arXiv:1909.11941 \[hep-ph\]](#).
- [55] Y.-P. Zeng, C. Cai, D.-Y. Liu, Z.-H. Yu, and H.-H. Zhang, “Probing quadruplet scalar dark matter at current and future pp colliders,” *Phys. Rev. D* **101** (2020) 115033, [arXiv:1910.09431 \[hep-ph\]](#).
- [56] N. F. Bell, M. J. Dolan, L. S. Friedrich, M. J. Ramsey-Musolf, and R. R. Volkas, “Two-Step Electroweak Symmetry-Breaking: Theory Meets Experiment,” *JHEP* **05** (2020) 050, [arXiv:2001.05335 \[hep-ph\]](#).
- [57] C.-W. Chiang, G. Cottin, Y. Du, K. Fuyuto, and M. J. Ramsey-Musolf, “Collider Probes of Real Triplet Scalar Dark Matter,” [arXiv:2003.07867 \[hep-ph\]](#).
- [58] S. Jangid and P. Bandyopadhyay, “Distinguishing Inert Higgs Doublet and Inert Triplet Scenarios,” *Eur. Phys. J. C* **80** (2020) 715, [arXiv:2003.11821 \[hep-ph\]](#).
- [59] P. Konar, A. Mukherjee, A. K. Saha, and S. Show, “A dark clue to seesaw and leptogenesis in singlet doublet scenario with (non)standard cosmology,” [arXiv:2007.15608 \[hep-ph\]](#).
- [60] N. G. Deshpande and E. Ma, “Pattern of Symmetry Breaking with Two Higgs Doublets,” *Phys. Rev.* **D18** (1978) 2574.
- [61] M. Ahmad *et al.*, “CEPC-SPPC Preliminary Conceptual Design Report. 1. Physics and Detector,” IHEP-CEPC-DR-2015-01, IHEP-TH-2015-01, IHEP-EP-2015-01.
- [62] **FCC** Collaboration, A. Abada *et al.*, “FCC Physics Opportunities: Future Circular Collider Conceptual Design Report Volume 1,” *Eur. Phys. J. C* **79** (2019) 474.
- [63] **CEPC Study Group** Collaboration, M. Dong *et al.*, “CEPC Conceptual Design Report: Volume 2 - Physics & Detector,” [arXiv:1811.10545 \[hep-ex\]](#).
- [64] **FCC** Collaboration, A. Abada *et al.*, “FCC-ee: The Lepton Collider: Future Circular Collider Conceptual Design Report Volume 2,” *Eur. Phys. J. ST* **228** (2019) 261–623.
- [65] H. Baer *et al.*, “The International Linear Collider Technical Design Report - Volume 2: Physics,” [arXiv:1306.6352 \[hep-ph\]](#).
- [66] J. Fan, M. Reece, and L.-T. Wang, “Possible Futures of Electroweak Precision: ILC, FCC-ee, and CEPC,” *JHEP* **09** (2015) 196, [arXiv:1411.1054 \[hep-ph\]](#).
- [67] K. Kumericki, I. Picek, and B. Radovcic, “Critique of Fermionic $R\nu$ MDM and its Scalar Variants,” *JHEP* **07** (2012) 039, [arXiv:1204.6597 \[hep-ph\]](#).
- [68] L. Di Luzio, R. Gröber, J. F. Kamenik, and M. Nardecchia, “Accidental matter at the LHC,” *JHEP* **07** (2015) 074, [arXiv:1504.00359 \[hep-ph\]](#).
- [69] Z.-H. Yu, J.-M. Zheng, X.-J. Bi, Z. Li, D.-X. Yao, and H.-H. Zhang, “Constraining the interaction strength between dark matter and visible matter: II. scalar, vector and spin-3/2 dark matter,” *Nucl. Phys. B* **860** (2012) 115–151, [arXiv:1112.6052 \[hep-ph\]](#).
- [70] J. R. Ellis, A. Ferstl, and K. A. Olive, “Reevaluation of the elastic scattering of supersymmetric dark matter,” *Phys. Lett. B* **481** (2000) 304–314, [arXiv:hep-ph/0001005](#).

- [71] **Particle Data Group** Collaboration, M. Tanabashi *et al.*, “Review of Particle Physics,” *Phys. Rev. D* **98** (2018) 030001.
- [72] A. Alloul, N. D. Christensen, C. Degrande, C. Duhr, and B. Fuks, “FeynRules 2.0 - A complete toolbox for tree-level phenomenology,” *Comput. Phys. Commun.* **185** (2014) 2250–2300, [arXiv:1310.1921 \[hep-ph\]](#).
- [73] J. Alwall, R. Frederix, S. Frixione, V. Hirschi, F. Maltoni, O. Mattelaer, H. S. Shao, T. Stelzer, P. Torrielli, and M. Zaro, “The automated computation of tree-level and next-to-leading order differential cross sections, and their matching to parton shower simulations,” *JHEP* **07** (2014) 079, [arXiv:1405.0301 \[hep-ph\]](#).
- [74] T. Sjöstrand, S. Ask, J. R. Christiansen, R. Corke, N. Desai, P. Ilten, S. Mrenna, S. Prestel, C. O. Rasmussen, and P. Z. Skands, “An introduction to PYTHIA 8.2,” *Comput. Phys. Commun.* **191** (2015) 159–177, [arXiv:1410.3012 \[hep-ph\]](#).
- [75] M. L. Mangano, M. Moretti, F. Piccinini, and M. Treccani, “Matching matrix elements and shower evolution for top-quark production in hadronic collisions,” *JHEP* **01** (2007) 013, [arXiv:hep-ph/0611129](#).
- [76] **DELPHES 3** Collaboration, J. de Favereau, C. Delaere, P. Demin, A. Giammanco, V. Lemaître, A. Mertens, and M. Selvaggi, “DELPHES 3, A modular framework for fast simulation of a generic collider experiment,” *JHEP* **02** (2014) 057, [arXiv:1307.6346 \[hep-ex\]](#).
- [77] M. Beltran, D. Hooper, E. W. Kolb, Z. A. Krusberg, and T. M. Tait, “Maverick dark matter at colliders,” *JHEP* **09** (2010) 037, [arXiv:1002.4137 \[hep-ph\]](#).
- [78] A. Rajaraman, W. Shepherd, T. M. Tait, and A. M. Wijangco, “LHC Bounds on Interactions of Dark Matter,” *Phys. Rev. D* **84** (2011) 095013, [arXiv:1108.1196 \[hep-ph\]](#).
- [79] P. J. Fox, R. Harnik, J. Kopp, and Y. Tsai, “Missing Energy Signatures of Dark Matter at the LHC,” *Phys. Rev. D* **85** (2012) 056011, [arXiv:1109.4398 \[hep-ph\]](#).
- [80] Z.-H. Yu, X.-J. Bi, Q.-S. Yan, and P.-F. Yin, “Detecting light stop pairs in coannihilation scenarios at the LHC,” *Phys. Rev. D* **87** (2013) 055007, [arXiv:1211.2997 \[hep-ph\]](#).
- [81] Q.-F. Xiang, X.-J. Bi, P.-F. Yin, and Z.-H. Yu, “Searches for dark matter signals in simplified models at future hadron colliders,” *Phys. Rev. D* **91** (2015) 095020, [arXiv:1503.02931 \[hep-ph\]](#).
- [82] **ATLAS** Collaboration, M. Aaboud *et al.*, “Search for new phenomena in final states with an energetic jet and large missing transverse momentum in pp collisions at $\sqrt{s} = 13$ TeV using the ATLAS detector,” *Phys. Rev. D* **94** (2016) 032005, [arXiv:1604.07773 \[hep-ex\]](#).
- [83] **ATLAS** Collaboration, M. Aaboud *et al.*, “Search for dark matter and other new phenomena in events with an energetic jet and large missing transverse momentum using the ATLAS detector,” *JHEP* **01** (2018) 126, [arXiv:1711.03301 \[hep-ex\]](#).
- [84] M. Low and L.-T. Wang, “Neutralino dark matter at 14 TeV and 100 TeV,” *JHEP* **08** (2014) 161, [arXiv:1404.0682 \[hep-ph\]](#).

- [85] G. F. Giudice, T. Han, K. Wang, and L.-T. Wang, “Nearly Degenerate Gauginos and Dark Matter at the LHC,” *Phys. Rev. D* **81** (2010) 115011, [arXiv:1004.4902 \[hep-ph\]](#).
- [86] S. Gori, S. Jung, and L.-T. Wang, “Cornering electroweakinos at the LHC,” *JHEP* **10** (2013) 191, [arXiv:1307.5952 \[hep-ph\]](#).
- [87] P. Schwaller and J. Zurita, “Compressed electroweakino spectra at the LHC,” *JHEP* **03** (2014) 060, [arXiv:1312.7350 \[hep-ph\]](#).
- [88] Z. Han, G. D. Kribs, A. Martin, and A. Menon, “Hunting quasidegenerate Higgsinos,” *Phys. Rev. D* **89** (2014) 075007, [arXiv:1401.1235 \[hep-ph\]](#).
- [89] H. Baer, A. Mustafayev, and X. Tata, “Monojet plus soft dilepton signal from light higgsino pair production at LHC14,” *Phys. Rev. D* **90** (2014) 115007, [arXiv:1409.7058 \[hep-ph\]](#).
- [90] A. Barr and J. Scoville, “A boost for the EW SUSY hunt: monojet-like search for compressed sleptons at LHC14 with 100 fb^{-1} ,” *JHEP* **04** (2015) 147, [arXiv:1501.02511 \[hep-ph\]](#).
- [91] **ATLAS** Collaboration, M. Aaboud *et al.*, “Search for electroweak production of supersymmetric states in scenarios with compressed mass spectra at $\sqrt{s} = 13 \text{ TeV}$ with the ATLAS detector,” *Phys. Rev. D* **97** (2018) 052010, [arXiv:1712.08119 \[hep-ex\]](#).
- [92] **Gfitter Group** Collaboration, M. Baak, J. Cúth, J. Haller, A. Hoecker, R. Kogler, K. Mönig, M. Schott, and J. Stelzer, “The global electroweak fit at NNLO and prospects for the LHC and ILC,” *Eur. Phys. J. C* **74** (2014) 3046, [arXiv:1407.3792 \[hep-ph\]](#).
- [93] M. E. Peskin and T. Takeuchi, “A New constraint on a strongly interacting Higgs sector,” *Phys. Rev. Lett.* **65** (1990) 964–967.
- [94] M. E. Peskin and T. Takeuchi, “Estimation of oblique electroweak corrections,” *Phys. Rev. D* **46** (1992) 381–409.
- [95] H.-H. Zhang, Y. Cao, and Q. Wang, “The Effects on S, T, and U from higher-dimensional fermion representations,” *Mod. Phys. Lett. A* **22** (2007) 2533–2538, [arXiv:hep-ph/0610094](#).
- [96] H.-H. Zhang, W.-B. Yan, and X.-S. Li, “The Oblique corrections from heavy scalars in irreducible representations,” *Mod. Phys. Lett. A* **23** (2008) 637–646, [arXiv:hep-ph/0612059](#).
- [97] P. Sikivie, L. Susskind, M. B. Voloshin, and V. I. Zakharov, “Isospin Breaking in Technicolor Models,” *Nucl. Phys. B* **173** (1980) 189–207.
- [98] **XENON** Collaboration, E. Aprile *et al.*, “Dark Matter Search Results from a One Ton-Year Exposure of XENON1T,” *Phys. Rev. Lett.* **121** (2018) 111302, [arXiv:1805.12562 \[astro-ph.CO\]](#).
- [99] B. Mount *et al.*, “LUX-ZEPLIN (LZ) Technical Design Report,” [arXiv:1703.09144 \[physics.ins-det\]](#).
- [100] G. Passarino and M. Veltman, “One Loop Corrections for $e^+ e^-$ Annihilation Into $\mu^+ \mu^-$ in the Weinberg Model,” *Nucl. Phys. B* **160** (1979) 151–207.

- [101] A. Denner, “Techniques for calculation of electroweak radiative corrections at the one loop level and results for W physics at LEP-200,” *Fortsch. Phys.* **41** (1993) 307–420, [arXiv:0709.1075 \[hep-ph\]](#).
- [102] T. Hahn and M. Perez-Victoria, “Automatized one loop calculations in four-dimensions and D-dimensions,” *Comput. Phys. Commun.* **118** (1999) 153–165, [arXiv:hep-ph/9807565](#).